Dynamic simulation on the synthetic reservoir CERENA I

Compositional fluid flow simulation with 4D seismic monitoring on a reservoir with a large content of CO_2

Pedro Tomás Madeira Pinto

Thesis to obtain the Master of Science Degree in

Petroleum Engineering

Supervisor: Doctor Leonardo Azevedo Guerra Raposo Pereira

Examination Committee

Chairperson: Professor Maria João Correia Colunas Pereira

Supervisor: Doctor Leonardo Azevedo Guerra Raposo Pereira

Members of the Committee: Doctor Maria Teresa Castro Bangueses Ribeiro

November 2014

This page was intentionally left blank

We choose to go to the moon. We choose to go to the moon in this decade and do the other things, not because they are easy, but because they are hard, because that goal will serve to organize and measure the best of our energies and skills, because that challenge is one that we are willing to accept, one we are unwilling to postpone, and one which we intend to win, and the others, too.

John Fitzgerald Kennedy

This page was intentionally left blank

Acknowledgments

The following work would not have been possible without the help and support of those mentioned below. For this reason I would like to express my most sincere gratitude to:

Doctor Leonardo Azevedo, my advisor, for the constant support and encouragement throughout this last year.

Professor Amílcar Soares, on behalf of CERENA, for the support and working conditions.

Doctor Teresa Ribeiro, from Partex Oil&Gas, for all the valuable insight and advice on how to approach and manage this reservoir, and also for her kind words of encouragement.

Professor António Costa Silva, chairman of Partex Oil&Gas, who was kind enough to put me in contact with Dra. Teresa Ribeiro when I approached him asking for textbook references in reservoir management.

Engº Víctor Alcobia, from Beicip Franlab, for the help and advice in the early stages of this work, when compositional simulation was simply overwhelming.

Engº José Ortiz, from Partex Oil&Gas, for the advice on gas cycling and surface facilities.

Professor Salgado Gomes, from the Petroleum Institute of Abu Dhabi, for the comprehensive saturation functions data set, which unfortunately I was not able to explore in due time.

I would also like to thank Dmitry Eydinov, from Rock Flow Dynamics, for providing me with a tNavigator® licence, and Schlumberger for the donation of academic licenses for Petrel® and Eclipse®.

Finally, a word of appreciation for my colleagues, who worked with me daily and bore with many of my doubts and dilemmas.

This page was intentionally left blank

Abstract

Dynamic simulation on a reservoir containing a large amount of CO_2

Compositional fluid flow simulation with 4D seismic monitoring on the synthetic reservoir CERENA-I

When it comes to Brazilian pre-salt reservoirs everything is huge: the reserves, the distances to shore and the investments as well. One particular field, Júpiter, also has a very large amount of CO_2 present. This poses great challenges in every aspect of reservoir production. The first part of this thesis focuses on the compositional fluid flow simulation of the synthetic reservoir CERENA-I, which mimics some characteristics of the Júpiter field, having a saturated oil leg with a retrograde condensation gas cap, both rich in CO_2. One of the main objectives of this work was to devise a production strategy that allowed the maximum gas cycling and storage. A dynamic model was built based on the CERENA-I reservoir, using bottom hole data borrowed from a neighbouring field. The production strategy was tailored for the best oil recovery while enabling the maximum storage of CO_2 back into the reservoir. The second part of this thesis uses the compositional simulation to model the changes in the seismic response of the reservoir during production. A rock physics model was created for specific time steps using the Xu-Payne methodology and a set of time-lapse seismic data was computed for each time step. The changes in seismic response were observed by subtracting the seismic volumes. For a better observation of the influence of pore fluids on the seismic response of the reservoir, seismic attributes such as the Lamé parameters were calculated and revealed distinct trends for each fluid type.

Keywords: Compositional fluid flow simulation, CO_2, gas cycling, synthetic reservoir, seismic monitoring, time-lapse seismic.

This page was intentionally left blank

Resumo

Simulação dinâmica num reservatório com uma grande quantidade de CO_2

Simulação composicional de fluidos com monitorização sísmica 4D no reservatório sintético CERENA-I

Os reservatórios do Pré-Sal Brasileiro apresentam grandes desafios associados: grandes reservas, grandes distâncias à costa, assim como grandes investimentos. Um campo em particular, Júpiter, contém ainda uma grande quantidade de CO_2 presente. Isto coloca grandes desafios à produção do reservatório. A primeira parte desta tese foca-se na simulação composicional de fluidos no reservatório sintético CERENA-I, que reproduz algumas características do campo Júpiter, tendo um anel de óleo saturado com um *gas cap* de condensação retrógrada, ambos com uma elevada concentração de CO_2. Um dos principais objectivos deste trabalho era o de desenvolver uma estratégia de produção que permitisse a ciclagem do maior volume de gás possível. O modelo de simulação dinâmica foi construído com base no reservatório CERENA-I, utilizando dados de pressão e temperatura de um reservatório real do Pré-Sal. A estratégia de produção foi ajustada para permitir a melhor recuperação de óleo, e também o máximo armazenamento de CO_2 no reservatório.

A segunda parte da tese usa a simulação composicional para modelar as alterações da resposta sísmica do reservatório durante a produção. Foi criado um modelo de física das rochas segundo a metodologia de Xu-Payne, que serviu de base para o cálculo de um conjunto de dados de sísmica 4D para os *time steps* seleccionados. As alterações na resposta sísmica foram observadas subtraindo os volumes sísmicos. Para uma melhor observação da influencia dos fluidos na resposta sísmica foram também calculados atributos sísmicos tais como os coeficientes de Lamé, que revelaram tendências distintas para cada tipo de fluido.

Palavras chave: Simulação composicional de fluidos, CO_2, ciclagem de gás, reservatório sintético, monitorização sísmica, sísmica 4D.

This page was intentionally left blank

Table of contents

List of Figures

List of Tables

List of equations

1. Introduction

1.1. Motivation

This thesis follows the path set during my internship as a Geomodeller at the Centre for Petroleum Reservoir Modelling, of Instituto Superior Técnico, in which a synthetic reservoir model was built to replicate some features of Brazilian Pre-Salt Reservoirs. Having acquired a useful set of modelling skills in static reservoir modelling, this thesis was seen as an opportunity to complement them with expertise in dynamic modelling as well as in rock physics and time-lapse seismic.

1.2. Objectives

The idea for this work came from a reservoir in the Brazilian Pre-Salt play with a very high content of CO_2. This reservoir poses great challenges in every aspect of its production, from reservoir modelling and management, to surface facilities. Figure 1 shows the Pre-Salt play where Júpiter, the real analogue for this study, can be found:

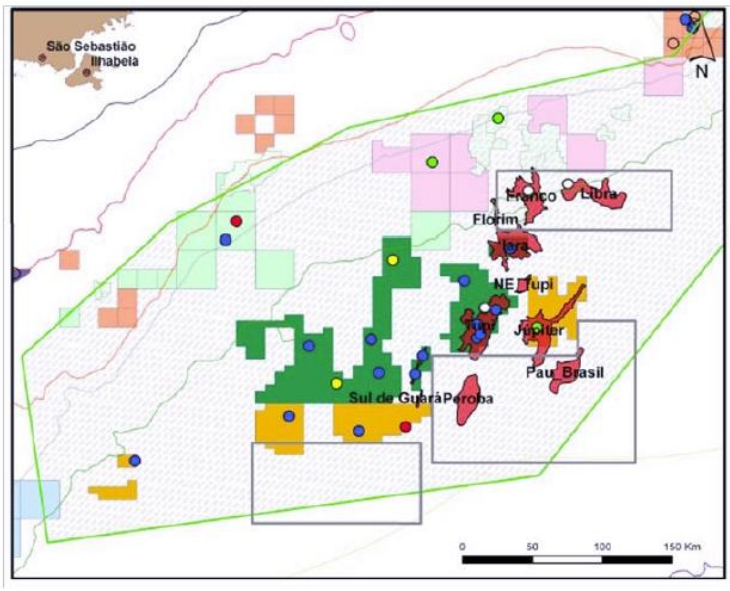

Figure 1: The Brazilian Pre-Salt Play (Source: ANP)

The reservoir covers an area of 567 km^2 about 300km offshore of Rio de Janeiro, in the Santos basin. It is situated in water depths of around 2000m, with the top of the reservoir situated at approximately 5200m. It has a 90m thick heavy oil leg with 18^o API and 55% (molar) of CO_2 content. It also has a gas cap of retrograde condensation gas which contains approximately 80% (molar) of CO_2.

The initial objective for the project was to create a dynamic compositional model based on the CERENA-I data set, to test reservoir performance and fluid behaviour under such conditions as stated above, as well as production strategies. As the work went on and the project matured, an additional objective

started to be within reach: the link between compositional reservoir simulation and rock physics models, with the creation of time-lapse seismic data set to mimic real time-lapse seismic monitoring.

1.3. Structure of the thesis

This work reflects a continuous process connecting several areas of Petroleum Engineering and the organization of this text tries to reflect that. This thesis is divided into three major parts: the introduction and theory, where the problem is introduced and the key theoretical concepts necessary to approach it are presented; the synthetic application, where the problem is addressed and results are shown as they are produced. Finally, some conclusions are presented, summing up an overall view of the work and its results.

1.4. Methodology

The methodology for this thesis can be basically divided into three major parts: the construction of the dynamic model, based on the CERENA-I static model; the dynamic simulation of the model, or the production of the field; and finally the calculation of synthetic time-lapse seismic models based on the dynamic simulation outputs.

The dynamic model was built recurring to the CERENA-I static model as a starting point. Reservoir conditions were borrowed from a neighbouring field from the Brazilian Pre-Salt play. Due to the lack of real data, fluid composition was obtained from Schlumberger's Petrel® fluids library and PVT behaviour, in order to match the estimated bubble point of the oil, was modelled through a tuned equation of state in Schlumberger's PVTi package.

The dynamic flow simulation was run in Schlumberger's Eclipse 300® and tNavigator® by Rock Flow Dynamics. The simulation code used for this work is available in section 7.

When a satisfying production scheme was achieved, several relevant simulated time steps were selected and, for each one, data relative to pore fluid densities, saturations and compressibility was retrieved and, together with a rock matrix elastic model, were used to calculate the evolution of the reservoir's elastic properties throughout the life of the field. These were later used to compute a set of time-lapse seismic volumes as well as an AVO analysis and seismic attributes.

A simplified schematic representation of the workflow previously described is presented in Figure 2.

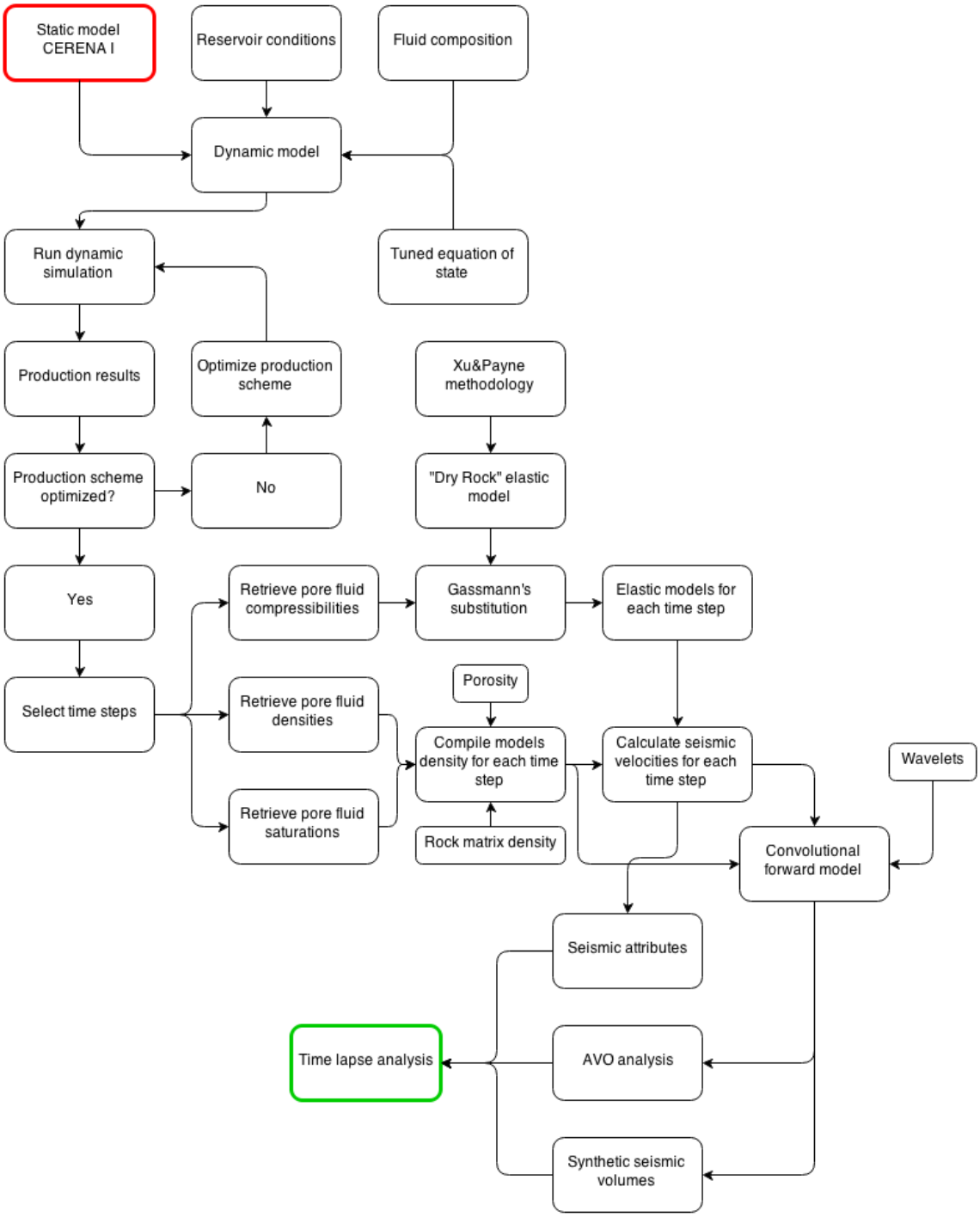

Figure 2: Schematic representation of the workflow used for the proposed methodology

2. State of the art and theoretical background

In this section, a brief summary of recent methods to deal with hydrocarbon reservoirs with a considerable amount CO_2 is presented. This is followed by the theoretical concepts needed to address this issue, such as reservoir compositional fluid flow simulation (Fanchi, 2006) and rock physics models (Avseth, Mukerji, & Mavko, 2005) (Mavko, Mukerji, & Dvorkin, 2009).

2.1. CO_2 storage

CO_2 is one of the most infamous greenhouse gases and the ever increasing pressure to cut down its emissions will force the oil companies that wish to operate fields with conditions such as those found in Júpiter to adopt strict environmental policies and practices.

In the Brazilian Pre-Salt Santos basin, Petrobras is currently undertaking a pilot CO_2 re-injection method to deal with the entire CO_2 produced in this basin, re-injecting it into Lula field in a WAG (water-alternating-gas) scheme. This works both as a CO_2 storage method and also an Enhanced Oil Recovery method (EOR), since Lula contains only 8-12% of CO_2 content. This project aims to inject 2000 tonnes of CO_2 per day (Araújo, 2013).

This type of integrated solutions will have to be continuously evolving, not only because as production increases also more CO_2 is produced, but because other fields with large CO_2 contents are being discovered, such as the giant field Libra with 40% of CO_2 (Lara, 2014).

Usually, CO_2 EOR processes are designed to optimize production while minimizing the amount of CO_2 necessary. Jessen et al, address the issue from an opposite perspective: how to use the greatest amount of CO_2 possible in an enhanced recovery mechanism. They ran a simulation case from which several conclusions can be borrowed to use in similar cases like this one:

1: Adjust injection gas composition to maximize CO_2 concentration while maintaining an appropriate minimum miscibility pressure.

2: Design well completions (or consider horizontal wells) to create injection profiles that reduce the adverse effects of preferential flow of injected gas through high permeability zones.

3: Optimize water injection (timing, injection rates and WAG ratio) to minimize gas cycling and maximize gas storage.

4: Consider aquifer injection to store CO2 that would flow rapidly to producing wells if re-injected in the oil zone.

5: Consider reservoir re-pressurization after the end of the producing life of the field.

2.2. Fluid flow simulators

Fluid flow simulators allow the simulation of fluid flow in porous media. In reservoir engineering, they are used to predict reservoir performance and plan reservoir management. Most reservoir simulators used are either Black Oil or Compositional simulators.

Compositional fluid flow simulators are substantially more complex than Black Oil simulators because they involve the calculation of fluid properties for the flow equations at every time step, whereas a Black Oil simulator simply reads them from input Tables. For this reason, Compositional fluid flow simulation also requires significantly more computational resources and time. Despite this complexity, the next section presents a simple comparison between both methods.

2.2.1. Black oil Vs. Compositional simulation

A detailed description of simulation methods would extend itself beyond the scope of this thesis so a practical comparison between them is presented instead. This section aims to point out the advantages of compositional simulation to the problem in hands.

In a black oil simulator, the conservation of mass applies to phases, whereas in compositional simulation it applies to components. Therefore, in the later, the mass of the various phases may vary in a time step but the mass of components is maintained. This can easily be understood by imagining the liberation of gas by an oil phase: oil looses mass as gas is liberated but the overall mass of, for instance, methane is maintained, as the sum of masses of this component in the gas and liquid phases.

Both black oil and compositional simulators solve multiphase, multidimensional flow equations for fluids whose properties depend on pressure. The flow equations for an oil, water, and gas system are determined by specifying the fluxes and concentrations of the conservation equations for each of the three components in each of the three phases. A flux in a given direction can be written as the density of the fluid times its velocity in the given direction.

This is where these two types of simulators diverge. In a black oil, pressure dependent properties for the flow equations, such as density, are simply read from an input Table, while in a compositional simulator they are calculated for every single time step as a function of pressure and composition, as can be seen in Figure 3.

$$\left.\begin{matrix} B_o \\ B_g \\ R_s \\ \mu \end{matrix}\right\} = f(p) \qquad \left.\begin{matrix} K_i = \dfrac{y_i}{x_i} \\ \mu \\ \rho \end{matrix}\right\} f(p, x_i, y_i)$$

Black oil **Compositional**

Figure 3: Differences between black oil and compositional simulators (adapted from Schlumberger, 2005)

In a compositional model, all we know is what components are present. We first have to calculate how many phases are present at the given pressure and temperature. If there are both oil and gas phases, we have to calculate the composition of each phase. Given these compositions we then have to calculate the physical properties of each phase independently, for example the oil viscosity.

The process of deciding how many phases are present, and their compositions, is called a "Flash". The flash calculation is based on the Rachford-Rice equation:

$$\sum_{i=1}^{N} \frac{Z_i(K_i - 1)}{1 + V(K_i - 1)} = 0$$ **Equation 1: Rachford-Rice equation**

Where Z_i is the total number of moles of the *i* component, K_i is the *K*-value for the *i* component and *V* is the unknown vapour molar fraction. Most of the CPU time required by a compositional fluid flow simulator can be spent in the flash calculations. Within the compositional fluid flow simulator, this is an iterative process performed for each component at every time step (Schlumberger, 2005).

Knowing the liquid and vapour molar compositions it is possible to calculate fluid properties using an Equation of State and the Lohrenz-Bray-Clark correlation (Lohrenz, Bray, & Clark, 1964).

An Equation of State is an analytic expression that relates volume to pressure and temperature. The simplest Equation of State is the Ideal Gas Law, in which the product of pressure and volume changes linearly with temperature:

$$PV = RT$$ **Equation 2: Ideal Gas Law**

For real gases, the deviation from ideal behaviour can be accounted for by the addition of the Z- factor, or compressibility factor:

$$PV = ZnRT$$ **Equation 3: Real Gas Law**

The most commonly used Equation of State for compositional problems is the Peng-Robinson equation:

$$P = \frac{RT}{(V - b)} - \frac{a}{V(V + b) + b(V - b)}$$ **Equation 4: Peng-Robinson Equation of State**

Where *a* and *b* are parameters inherited from the Van der Waals equation, to respectively account for the attractive force between molecules and the finite volume of molecules.

Despite the significantly greater complexity and computational requirements when compared to a Black Oil simulator, compositional simulation provides several clear advantages that the first simply cannot

match: phase behaviour; multi-contact miscibility; immiscible or near-miscible displacement behaviour in compositionally dependent mechanisms such as vaporisation, condensation, and oil swelling; composition-dependent phase properties such as viscosity and density on miscible sweep-out; interfacial Tension (IFT) especially the effect of IFT on residual oil saturation (Schlumberger, 2005).

2.3. Rock physics

A rock physics model establishes the relation between the rock's petro-physical properties and its petro-elastic properties (Mavko, Mukerji, & Dvorkin, 2009). It forms the foundation for seismic velocities prediction and subsequent seismic amplitude models, and it also relates the isotropic elastic moduli, K and μ, with rock properties such as porosity, mineral composition and grain arrangement.
The Bulk modulus, K, can be described as the extent to which a rock can be squashed and is defined as the ratio between the hydrostatic stress to the volumetric strain (Simm & Bacon, 2014):

$$K = \frac{S}{\Delta V/V}$$ **Equation 5: Bulk modulus**

Where S is the uniform compressive stress applied to the rock, and $\Delta V/V$ is the correspondent fractional volume change.

The shear modulus, or μ, relates to the rock's resistance movement in a direction that is perpendicular to the one in which energy is propagating (Simm & Bacon, 2014), and is defined as:

$$\mu = \frac{shear\ stress}{shear\ strain}$$ **Equation 6: Shear modulus**

P-wave velocity, or compressional wave velocity, can be described as a function of a medium's bulk and shear modulus, through the following relation:

$$V_p = \sqrt{\frac{K + \frac{4\mu}{3}}{\rho}}$$ **Equation 7: P-wave velocity**

The same applies to shear-wave velocity, which can be described through the following relation:

$$V_s = \sqrt{\frac{\mu}{\rho}}$$ **Equation 8: S-wave velocity**

Since fluids have no resistance to shear strain, the global shear modulus of a rock remains the same whatever type of fluid it may contain (oil, gas or water).

Rocks are never composed of a single continuous crystal. Even in pegmatites, igneous rocks on which several meter long crystals are sometimes found, crystals are finite and mineralogy is not constant. Most reservoir rocks fall within the micrometre or millimetre range of crystal size and are composed of several minerals. The interaction of particles with different properties and shapes with the pore space leads to the rock having global elastic moduli which differs significantly from a simple average of properties. This is the function of the rock physics model: to reproduce the interaction between rock components and determine its overall elastic moduli (Simm & Bacon, 2014).

Most rock physics models used can be grouped in four types: theoretical bounds; empirical models; contact models; and inclusion models.

Theoretical bounds establish the physical limits of mixtures of minerals and fluids (Simm & Bacon, 2014)without any requirements regarding grain shape, as they only predict the "stiffest" and "softest" elastic moduli possible, for the given components. The best bounds for an isotropic linear elastic dual component composite, giving the narrowest moduli range without any geometry requirements are the Hashin-Shtrikman bounds (Mavko, Mukerji, & Dvorkin, 2009), given by equations 5 and 6:

$$K^{HS\pm} = K_1 + \frac{f_2}{(K_2 - K_1)^{-1} + f_1(K_1 + \frac{4}{3}\mu_1)^{-1}}$$

Equation 9: Hashin-Shtrikman's Bulk modulus bounds

$$\mu^{HS\pm} = \mu_1 + \frac{f_2}{(\mu_2 - \mu_1)^{-1} + 2f_1(K_1 + 2\mu_1)/[5\mu_1(K_1 + \frac{4}{3}\mu_1)]}$$

Equation 10: Hashin-Shtrikman's Shear modulus bounds

Where K_1 and K_2 are the bulk moduli of each component, μ_1 and μ_2 are the shear moduli of each component, and f_1 and f_2 are the percentages of each component.

Empirical models are derived from fits made to experimental results. Generally they are simple mathematical relations involving two or three variables and result from regressions fitted to observations (Simm & Bacon, 2014).

Contact models are based on the mathematical principles of the interaction of granular materials and apply mainly to sandstones (Simm & Bacon, 2014). The two most commonly used contact models are the "friable sand" and the "cemented sand" models developed by Dvorkin and Nur (1996).

Inclusion models treat the rock as an elastic medium containing inclusions and are usually based on the Kuster-Toksöz theory, which requires pore concentration to be diluted so that no interaction occurs between pores. Xu and White (1996) addressed this issue and used an effective medium approach, in which the properties of the medium are calculated in stages, adding the porosity in small steps so that the diluted porosity condition of the Kuster-Toksöz theory is satisfied (Simm & Bacon, 2014). An example is the Differential Effective Medium model, shown in equations 7 and 8:

$$(1-y)\frac{d}{dy}[K^*(y)] = (K_2 - K^*)P^{(*2)}(y)$$ **Equation 11: Differential Effective Medium equation for Bulk modulus**

$$(1-y)\frac{d}{dy}[\mu^*(y)] = (\mu_2 - \mu^*)Q^{(*2)}(y)$$ **Equation 12: Differential Effective Medium equation for Shear modulus**

With initial conditions $K^*(0)= K_1$ and $\mu^*(0)= \mu_1$, where K_1 and μ_1 are the bulk and shear moduli of the initial host material, K_2 and μ_2 are the bulk and shear moduli of the incrementally added inclusion, and y is the increasing porosity. (Mavko, Mukerji, & Dvorkin, 2009)

Another important concept in rock physics modelling is Gassmann's equation. It allows some understanding of how the global bulk modulus of a rock is affected by changes in pore fluids, according to the following equation:

$$\frac{K_{sat}}{K_0 - K_{sat}} = \frac{K_d}{K_0 - K_d} + \frac{K_{fl}}{\emptyset\left(K_0 - K_{fl}\right)}$$ **Equation 13: Gassmann's relation**

where K_{sat} is the bulk modulus of the fluid-saturated rock, K_0 is the bulk modulus of the mineral matrix, K_d is the bulk modulus of the dry rock, K_{fl} is the bulk modulus of the fluid and $\emptyset$ is the porosity.

When seismic waves travelling in the sub-surface encounter a transition from a medium 1 to a medium 2 with different properties, part of the energy is reflected and the rest is transmitted. For normal incidence waves, the reflection coefficient at the interface between two different geological layers is given by:

$$R = \frac{(Z_1 - Z_0)^2}{(Z_1 + Z_0)^2}$$ **Equation 14: Normal incidence reflectivity**

where Z_1 and Z_2 are the acoustic impedances of the media, given by the product of density and P-wave velocity:

$$Z = V_p\rho$$ **Equation 15: Acoustic impedance**

When the incident wave reaches the media interface at any angle different from the perpendicular, the partitioning of energy into reflected and transmitted waves assumes a rather complex behaviour.

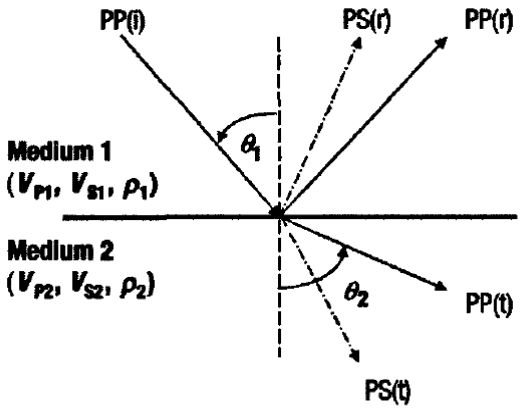

Figure 4: Partitioning of incident P-waves

This partitioning of P-waves into refracted and reflected S and P-waves (Figure 4) is accurately described by the Zoeppritz (1919) equations. These equations are often too complex for a straightforward use in reservoir geophysics so, for P-wave reflection analysis, Aki and Richards (1980) developed a well known approximation:

$$R(\theta_1) \approx \frac{1}{2}(1 - 4\rho^2 V_s^2)\frac{\Delta\rho}{\rho} + \frac{1}{2cos^2\theta}\frac{\Delta V_p}{V_p} - 4\rho^2 V_s^2 \frac{\Delta V_s}{V_s}$$ **Equation 16: Aki&Richards approximation**

where:

$p = \frac{sin\theta_1}{V_{P1}}$ $\theta = (\theta_1 + \theta_2)/2 \approx \theta_1$

$\Delta\rho = \rho_2 - \rho_1$ $\rho = (\rho_1 + \rho_2)/2$

$\Delta V_P = V_{P2} - V_{P1}$ $V_P = (V_{P2} + V_{P1})/2$

$\Delta V_s = V_{S2} - V_{S1}$ $V_S = (V_{S2} + V_{S1})/2$

Shuey (1985) developed a further approximation:

$$R(\theta) \approx R(0) + Gsin^2\theta + F(tan^2\theta - sin^2\theta)$$ **Equation 17: Shuey approximation**

where:

$R(0) = \frac{1}{2}(\frac{\Delta V_p}{V_p} + \frac{\Delta_\rho}{\rho})$

$$G = \frac{1}{2}\frac{\Delta V_p}{V_p} - 2\frac{V_s^2}{V_P^2}\left(\frac{\Delta \rho}{\rho} + 2\frac{\Delta V_s}{V_s}\right)$$

$$= R(0) - \frac{\Delta \rho}{\rho}\left(\frac{1}{2} + \frac{2V_s^2}{V_p^2}\right) - \frac{4V_s^2}{V_p^2}\frac{\Delta V_s}{V_s}$$

$$F = \frac{1}{2}\frac{\Delta V_p}{V_p}$$

Usually, the range of offsets available in seismic studies only goes up to 40^o so the *F* term can be discarded, and the approximation simplified to:

$$R(\theta) \approx R(0) + G sin^2\theta$$ **Equation 18: Two term Shuey approximation**

Where R(0) is the zero-offset reflectivity and G represents the change in reflectivity with increasing offset.

3. Dynamic simulation on the CERENA-I reservoir: Synthetic application

3.1. CERENA-I : Dataset description

The CERENA-I model was created to replicate some key characteristics of the Brazilian Pre-salt carbonate fields. This model contains high-resolution data sets of petro-physical and petro-elastic properties. It is based on a corner-point grid with 161x161x300 cells, with 25x25x1m spacing. For the case study presented herein only the sets of porosity and permeability were used. These models are based on a geological facies model which tries to translate the evolution of sedimentary environments on the early stages of a carbonate basin. The model is composed of two facies: a reservoir facies, composed by microbiolites; and a non-reservoir facies composed by mudstones. These are located in three distinct stratigraphic units of approximately 100 metres thickness, as shown in Figure 5. The lower unit is strongly laminated, representing inter-tidal or lagoon environments. The middle unit contains dome-shaped geometries representing reef formations. The top unit is composed of lenticular bodies (Figure 5).

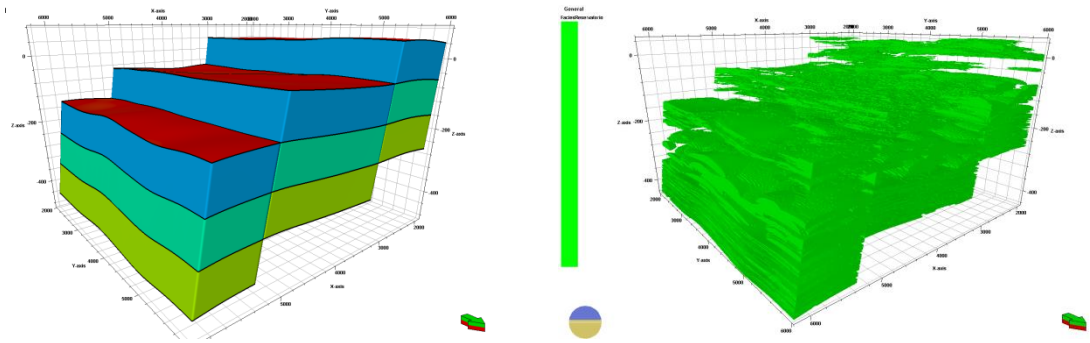

Figure 5: Stratigraphic units model (left) and geometries of the reservoir facies (right)

A porosity model was derived from the facies model recurring to stochastic sequential simulation and it is shown in Figure 6.

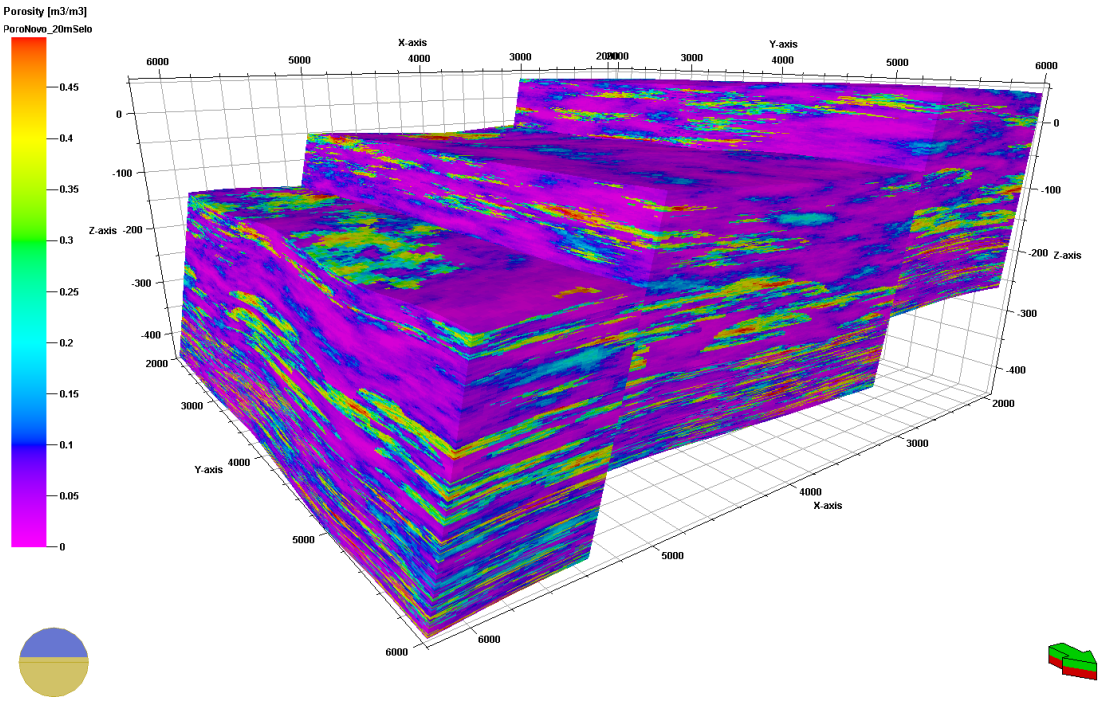

Figure 6: Porosity model

It is clear that there are two different porosity distributions in the model: one with low values with high spatial continuity; and another with higher values and much more heterogeneous. These correspond to the facies already described. This effect is clearly interpreted on the marginal distribution of porosity for the entire model (Figure 7). It is clear that the presence of two distinct families corresponding to the reservoir and non-reservoir facies.

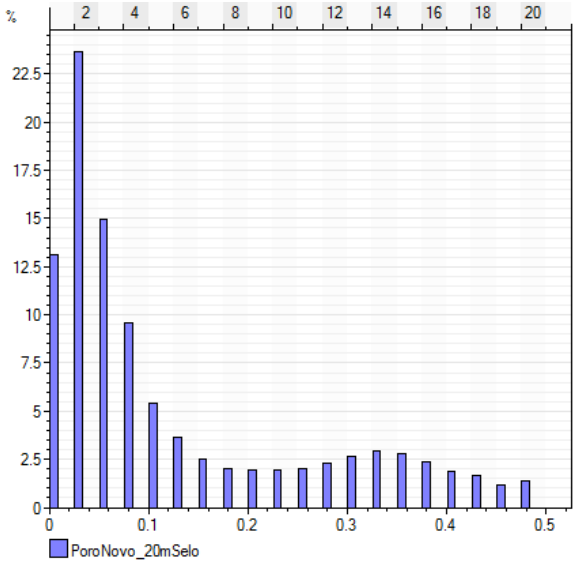

Figure 7: Histogram of porosity for both facies

Permeability was modelled recurring to the porosity model and it exhibits a dependence that was derived from real analogues (Kansas Geological Survey, 2004). The joint distribution between both properties can be seen in Figure 8.

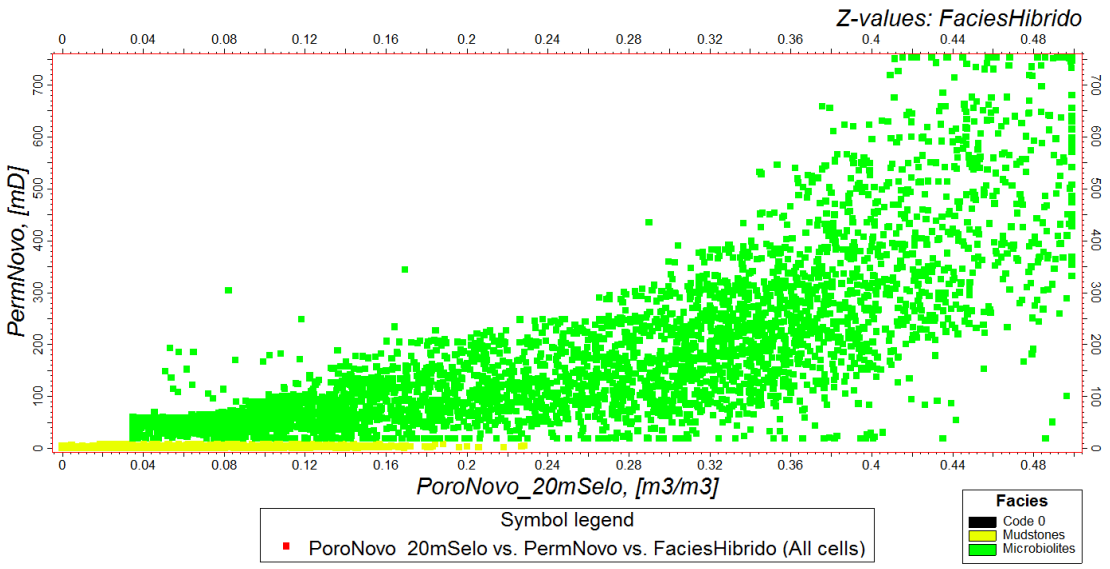

Figure 8: Joint distribution of porosity and permeability for both facies of the CERENA-I model

The permeability model reflects the behaviour already interpreted for the porosity. It can be seen that both facies exhibit very distinct characteristics, with the mudstones facies having a very tight behaviour, and the reservoir facies showing a very heterogeneous and exponential-type relation typical of carbonate reservoirs (Mavko, Mukerji, & Dvorkin, 2009). The histogram of permeability for the complete model is shown in Figure 9.

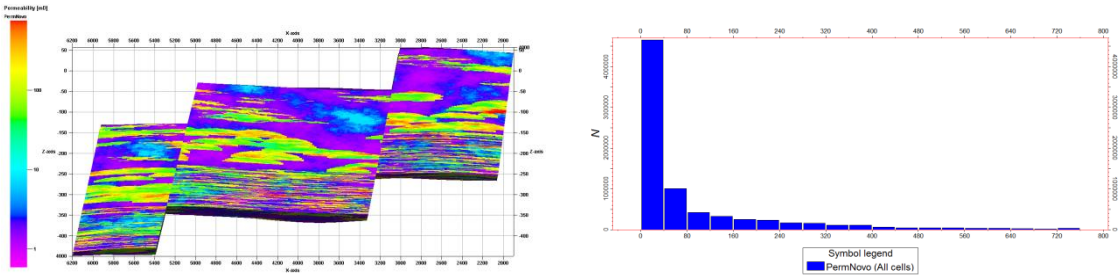

Figure 9: North view of the permeability model (left) and histogram of permeability (right)

As expected, there is a clear dominance of low permeability values due to the high homogeneity of the mudstones (non-reservoir) facies.

3.2. Fluids system

The definition of the fluid system is a crucial part of any compositional fluid flow simulation. This stage it is where the fluid PVT behaviour is tuned through an equation of state, so that the simulation reproduces, as closely as possible, the real phenomena that occur during reservoir production. In the following sub-sections the fluid composition is presented and the equation of state is tuned to match estimated parameters, after which several experiments are calculated and reported.

3.2.1. Fluid characterization

Due to the lack of real data from analogue fields the oil composition for this study was obtained from a generic sample of oil from Petrel® library. Table 1 presents the fluid composition.

Table 1: Molar percentages of the original oil sample

Component	Molar %	Mol. weight
N_2	0.16	28.013
CO_2	0.91	44.01
C_1	36.47	16.043
C_2	9.67	30.07
C_3	6.95	44.097
NC_4	3.93	58.124
IC_4	1.44	58.124
NC_5	1.41	72.151
IC_5	1.44	72.151
C_6	4.33	84
C_{7+}	33.29	218

The components distribution according to molecular weight is shown in Figure 10.

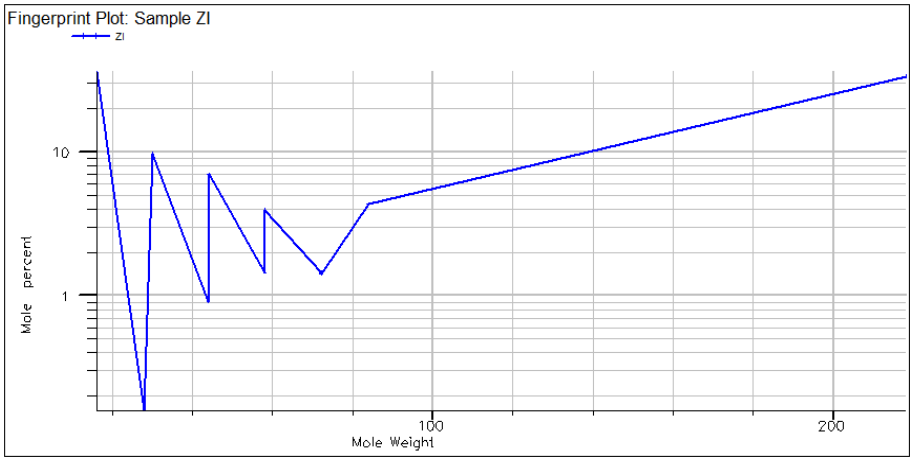

Figure 10: Molar percentages of the original oil sample

It can be seen that the distribution of components by molecular weight has an increasing trend. Usually this does not provide a good description of a fluid and can lead to significant differences between real and simulated fluid behaviour but for this case, with no real data to honour, it is considered sufficient.

The components were grouped to reduce computation time and memory requirements, and the molar percentages were re-adjusted to the known CO_2 content of the analogue field (Table 2).

Table 2: Molar percentages of the oil with grouped components

Component	Molar %	Mol. weight
CO_2	55.00	44.01
C_1	16.56	16.043
C_2	4.46	30.037
C_3	3.15	44.097
C_{4-6}	5.69	70.237
C_7^+	15.11	218

The C_7^+ fraction corresponds to an average weight of the components larger than C_7. Usually, in compositional simulation, this fraction is split into decreasing percentages of heavier components to produce a more realistic description of the heavy ends. In this case, since it's a synthetic model with no real data to honour, the heavier fraction was not split, to minimize the number of components and keep the memory requirements low.

The grouped sample's components distribution according do molecular weight (Figure 11) show the same overall behaviour of the one presented in Figure 10.

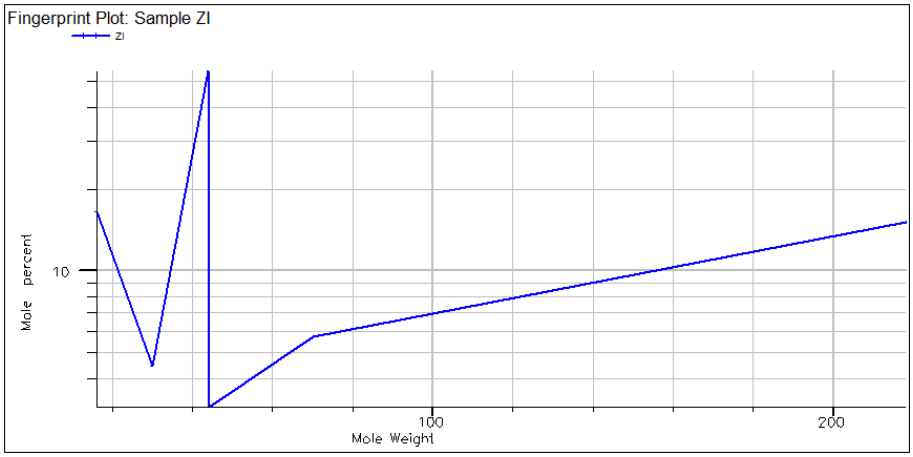

Figure 11: Molar percentages of the oil with grouped components

3.2.2. The Equation of State

The equation of state is a mathematical expression that relates variables such as pressure and volume of a given substance through several constants inherent to the substance (Schlumberger, 2005). When in a mixture, individual components influence each other and behave differently from when in pure substance. For that reason their constants should be tailored so that the equation reproduces real observed fluid behaviour. This process is called tuning the equation of state, and it's one of the most important and hardest steps in the creation of a compositional model. The process of tuning the Equation of state becomes harder with increase in the number of behaviour variables to be reproduced. For this case, the Equation of State is intended to honour an estimated bubble point and dew point (Table 3).

Table 3: Estimated observations

Bubble point (bar)	Dew point (bar)
493	400

Generally, when there is a gas phase present within a reservoir, the bubble point of the oil corresponds to the pressure at the gas-oil contact. This was estimated from the bottom hole pressure of a neighbouring Pre-Salt analogue, subtracting the litho-static pressure exerted by the 90 meters of oil leg, at a temperature of 100^{o}C. The dew point for the gas was assumed as being 400bar(a) to ensure that the entire gas cap was in supercritical conditions when the model was initialized.

For this case study, the three parameter Peng-Robinson equation of state was chosen as it is the most commonly used in the oil industry, and provides a more accurate calculation of phase density.

The regression was performed, adjusting critical pressures and temperatures for all components (Table 4).

Table 4: Calculated observations

Bubble point (bar)	Dew point (bar)
492.9964	399.9967

The regression is considered validated since there are only small differences between the calculated and estimated observations. Table 5 contains the tuned critical temperature and pressure for each of the oil components.

Table 5: Tuned critical properties for the oil components

Component	Critical pressure (bar)	Critical temperature ^{o}C
CO_2	119.19	-22.239
C_1	74.296	-116.2
C_2	78.417	-24.04
C_3	68.835	31.369
C_{4-6}	56.823	107.47
C_7^+	27.546	340.27

Having the Equation of State correctly tuned it is possible to calculate phase behaviour as a function of temperature and pressure (Figure 12).

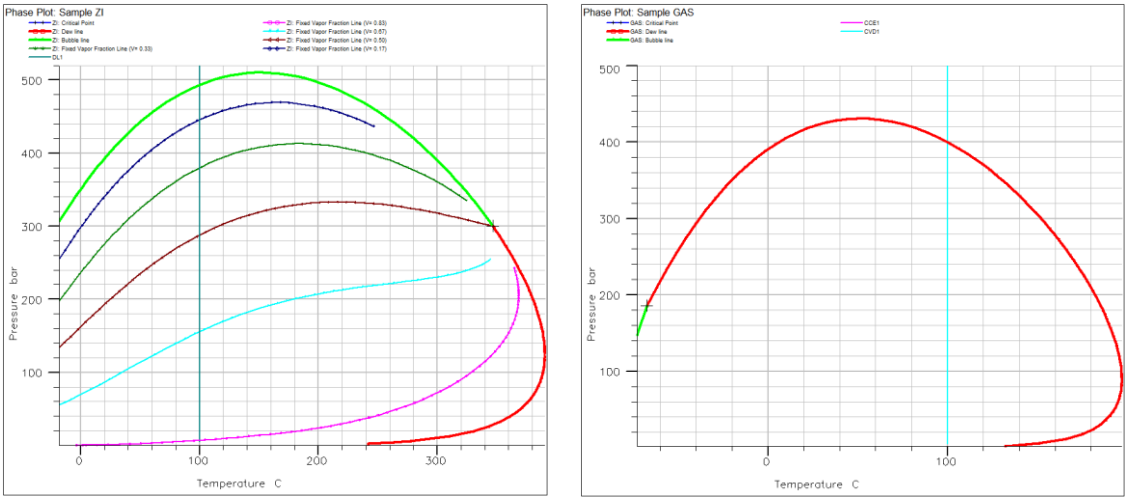

Figure 12: Phase plots for the oil (left) and gas cap (right)

3.2.3. Laboratory experiments

In real reservoir studies, laboratory experiments on reservoir fluid samples provide data for a detailed tuning of the equation of state. It is possible to tune the equation to reproduce not only observed saturation pressures (bubble or dew point) but also, for example, observed liquid/vapour compositions, field separator output fractions and compositions.

In this case, as only saturation pressures for gas and oil were used for regression, the remaining details of both experiments, as well as the other experiments, are simply calculated and reported to provide a description of expected fluid behaviour.

3.2.3.1. Bubble Point report

This experiment simulates the appearance of the first dissolved gas bubble, from a single liquid phase. The fluid sample is placed in a PVT cell at reservoir pressure and temperature, and pressure is dropped until the first bubble appears. According to Table 6, the bubble point was estimated at 492.99 bar:

Table 6: Calculated bubble point

Reservoir temperature (°C)	Bubble point (bar)
100	492.9964

This experiment also allows the calculation of fluid properties and compositions (Tables 7 and 8).

Table 7: Fluid properties at the bubble point

Fluid properties	Liquid	Vapour
Mole weight	66.5707	46.2729
Z-factor	1.2276	0.9694
Viscosity (cP)	0.8270	0.1932
Density (g/cm^3)	0.8617	0.7585

Table 8: Fluid components at the bubble point

Component	Liquid fraction	Vapour fraction	K-values
CO_2	54.9702	63.1585	1.1490
C_1	16.5732	20.3851	1.2300
C_2	4.4671	4.7362	1.0603
C_3	3.1583	2.9862	0.9455
C_{4-6}	5.7031	4.4493	0.7801
C_7^+	15.1281	4.2853	0.2833

3.2.3.2. Dew Point report

This experiment simulates the appearance of the first liquid drop from a retrograde condensation gas. The fluid is placed in a PVT cell at reservoir pressure and temperature, and pressure is dropped until the first droplet appears. According to Table 9, at reservoir temperature, this occurs at 399.99 bar:

Table 9: Calculated dew point

Reservoir temperature (^{o}C)	Dew point (bar)
100	399.9967

This experiment also allows the calculation of fluid properties and compositions (tables 10 and 11).

Table 10: Fluid properties at the dew point

Fluid properties	Liquid	Vapour
Mole weight	66.5707	46.2729
Z-factor	1.2276	0.9694
Viscosity	0.8270	0.1932
Density (g/cm^3)	0.8617	0.7585

Table 11: Fluid components at the dew point

Component	Liquid fraction	Vapour fraction	K-values
CO_2	54.9702	65.0408	1.1832
C_1	16.5732	22.0257	1.3289
C_2	4.4671	4.6550	1.0420
C_3	3.1583	2.7387	0.8671
C_{4-6}	5.7031	3.6636	0.3289
C_7^+	15.1281	1.8762	0.2833

3.2.3.3. Field separators report

This experiment simulates the fractioning that the fluid experiences in a field separator at specified conditions. Without any particular conditioning, the field separator conditions were set to the standard atmospheric conditions (Table 12).

Table 12: Surface separator conditions

Temperature (^{o}C)	Pressure (bar)
15.5	1.0132

The experiment was performed for both the oil leg and the gas cap to predict the characteristics of the fluid fractioning for both cases. The following Table refers to the properties of fluids fractioned from the reservoir in the field separator:

Table 13: Properties of fluids fractioned from the oil leg and gas cap

Fluid properties	Liquid	Vapour	Fluid properties	Liquid	Vapour
Mole weight	217.7783	39.5751	Mole weight	216.3791	38.0953
Z-factor	0.0107	0.9977	Z-factor	0.0107	0.9980
Viscosity	2.2963	0.0223	Viscosity	2.2787	0.0227
Density (g/cm^3)	0.8541	0.0017	Density (g/cm^3)	0.8538	0.0016
GOR (sm^3/sm^3)	518.5556		GOR (sm^3/sm^3)	4910.9792	
Properties of fluids separated from the oil leg			**Properties of fluids separated from the gas cap**		

Fluid compositions at separator conditions can also be calculated, and are shown in Tables 14 and 15 below:

Table 14: Molar distributions of the oil leg in the field separator

Component	Liquid fraction	Vapour fraction	K-values
CO_2	0.3255	64.8568	199.2385
C_1	0.0425	19.5640	460.5648
C_2	0.0428	5.2676	123.1727
C_3	0.0867	3.7141	42.8418
C_{4-6}	0.9058	6.5711	7.2549
C_7^+	98.5968	0.0264	0.0003

Table 15: Molar distributions of the gas cap in the field separator

Component	Liquid fraction	Vapour fraction	K-values
CO_2	0.3325	66.2732	199.2980
C_1	0.0487	22.4443	460.8207
C_2	0.0385	4.7429	123.2213
C_3	0.0651	2.7896	42.8528
C_{4-6}	0.5133	3.7236	7.2547
C_7^+	99.0019	0.0265	0.0003

3.2.3.4. Differential Liberation report

In this experiment a fixed volume of oil is expanded and the liberated gas is removed. This trial intends to simulate the changes in oil properties as pressure drops during production. The data resulting from this experiment is presented in graphics for a better observation of fluid behaviour. Starting with the evolution of reservoir oil viscosity with the pressure drop (Figure 13) it is seen that the oil experiences an almost constant increase in viscosity from the 0.8270 cP at the bubble point, to 2.3256 cP at surface conditions.

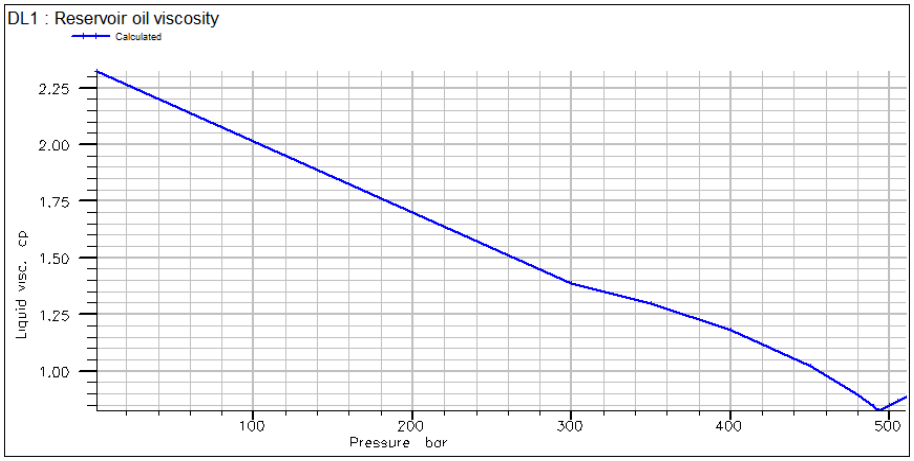

Figure 13: Reservoir oil viscosity as a function of pressure

Figure 14 shows the evolution of reservoir oil density with the pressure drop, where it can be seen that it reaches a minimum density of 0.8385 g/cm^3 at 300bar. Although the reservoir oil density is expected to change during the production, the maximum difference should not exceed 0.03 g/cm^3.

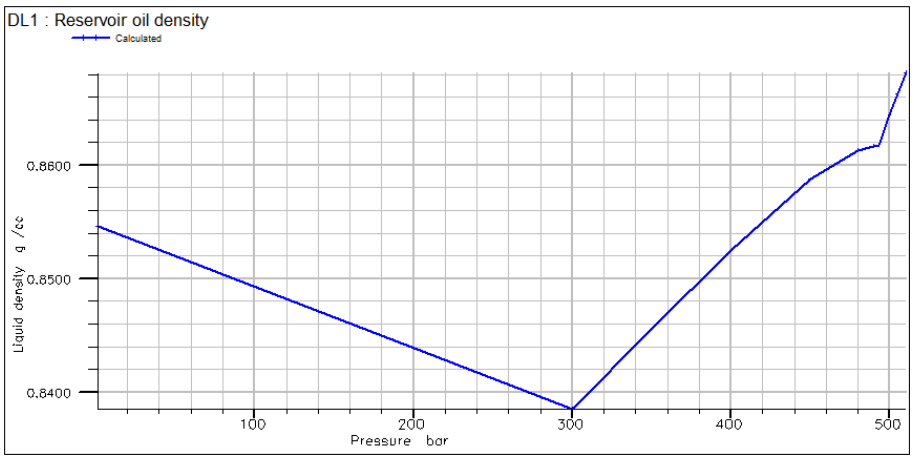

Figure 14: Reservoir oil density as a function of pressure

The most important factor influencing the changes in the reservoir oil viscosity is perhaps the amount of gas dissolved, or the solution gas-oil ratio. Figure 16 shows the evolution of this parameter as a function of pressure:

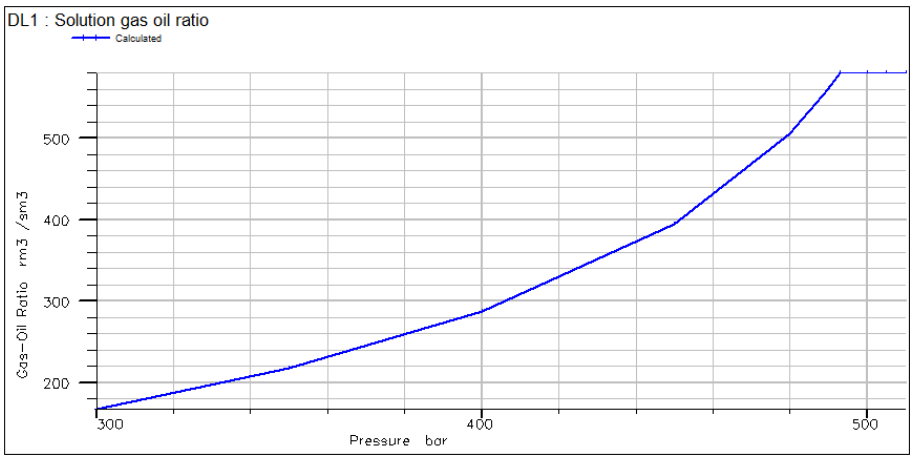

Figure 15: Gas-Oil ratio as a function of pressure

The solution gas-oil ration remains constant at 581 rm^3/sm^3 until the pressure drops below the bubble point, after which it declines to just under 200 rm^3/sm^3 at 300 bar.

3.2.3.5. Constant Volume Depletion report

The constant volume depletion experiment intends to replicate the conditions to which a gas is exposed during production with natural depletion. A defined volume of gas is depressurized past the dew point, to assess the changes in the gas properties and also on the condensate fraction. Figure 16 shows the evolution of liquid condensate density as a function of pressure. It is clear that the density of the condensate dropout decreases with the pressure drop, as heavier components condensate first.

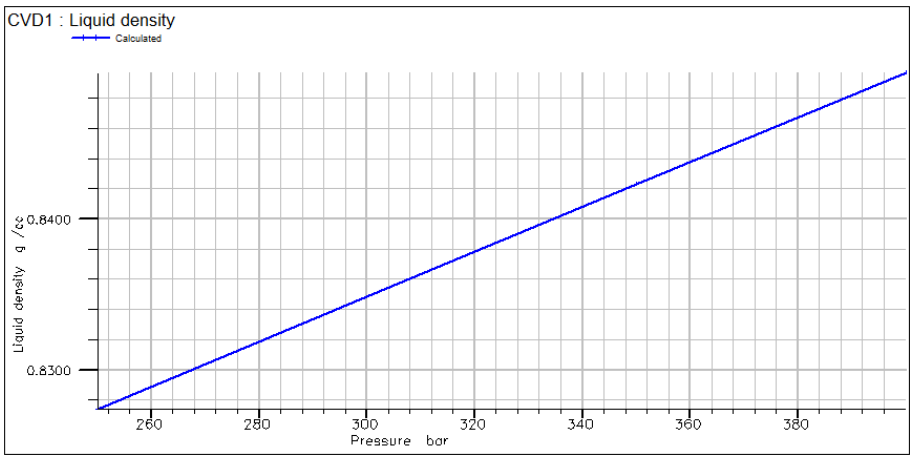

Figure 16: Liquid condensate density as a function of pressure

As expected, gas viscosity is correlated with pressure, and drops as pressure is reduced (Figure 17).

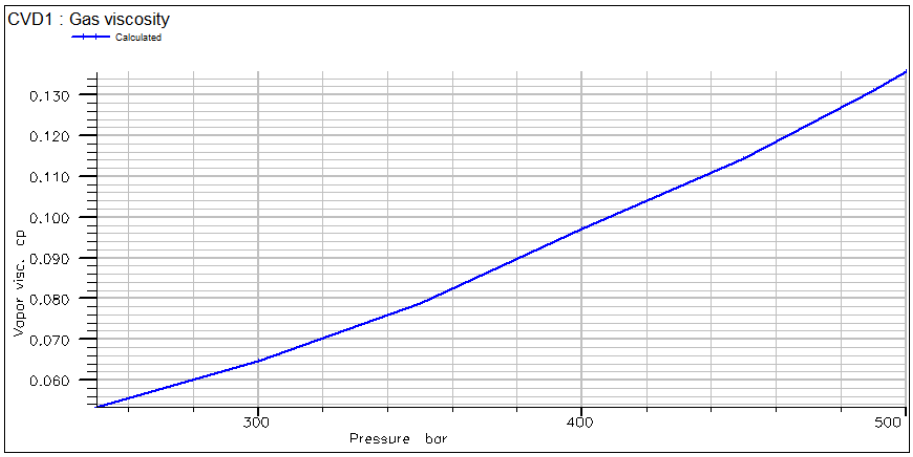

Figure 17: Gas viscosity as a function of pressure

3.2.3.6. Minimum Miscibility Pressure report

When dealing with multiphase reservoirs, and particularly with gas injection, it is important to know the conditions at which the gas dissolves in the oil, so this can either be achieved or avoided, depending on the objectives and the production scheme. The Multi-contact miscibility pressure for the field separator gas in the reservoir oil is given in Table 16.

Table 16: Minimum miscibility pressure

Temperature (°C)	MCMP[1] (bar)
100	536.0717

In this case, the injection process is intended for re-injecting the gas back into the reservoir. In order to avoid producing the injected gas in a continuous loop, the gas must not contact the oil at a pressure higher than 536 bar.

[1] Multi-Contact miscibility pressure

3.3. Dynamic model

3.3.1. Sectorial model

Since the final objective of this thesis was to produce time-lapse synthetic seismic volumes, the choice was made to run the simulation on a fine grid sectorial model which, despite being considerably smaller, reproduced the total variability of the full field, instead of an up scaled model. This option was taken so that a dynamic model could be run and still maintain a high resolution in the final seismic models. From this point on, the link to the original full field model is severed and the study object is now the sectorial model. For this reason no boundary effects will be added to the dynamic model, to account for the influence of the remaining area.

From the 16km^2 and 7million cell full field model, a 1km^2 and 280.000 active cells model was created, containing active cells only for the reservoir facies (Figure 18). This was chosen due to computational constraints. The resulting petro-physical sectorial models are shown in Figure 19.

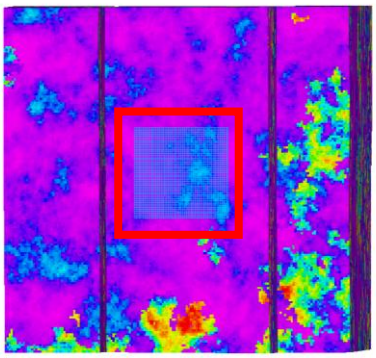

Figure 18: Sectorial model area

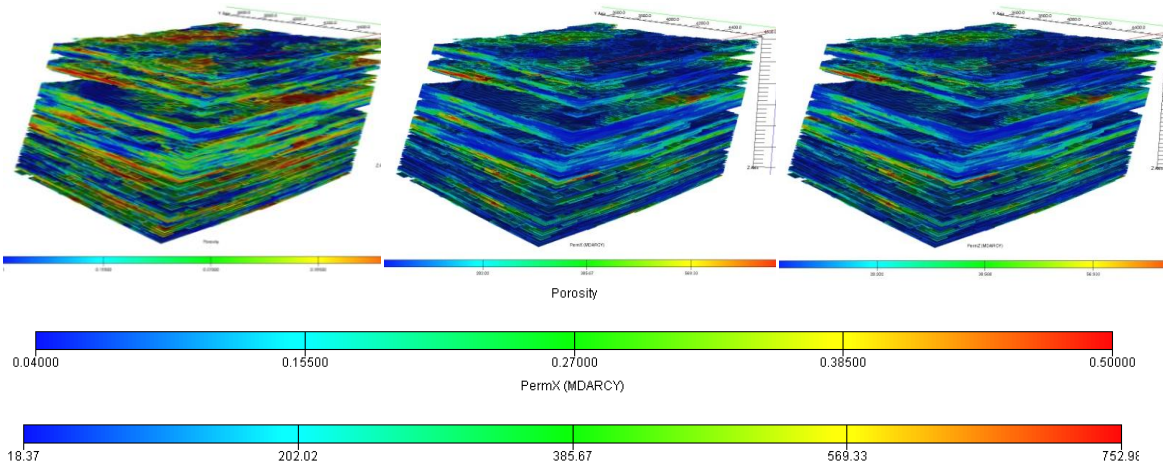

Figure 19: Porosity (left), horizontal (centre) and vertical (right) permeability models

The permeability was assumed to be isotropic in the horizontal directions while the vertical permeability was computed as 10% of the total horizontal permeability.

3.3.2. Model initialization

The compositional model was initialized providing the simulator with the pressure and depth of the gas-oil contact, the depth of the oil-water contact and the oil composition versus depth. The information regarding the model constraints is synthesized in Table 17.

Table 17: Contact depths

Oil-Water contact depth (m)	Gas-oil contact depth (m)	Gas-oil contact pressure (bar)
300	210 m	492.9964 bar

The saturation functions used in this simulation were borrowed from a classroom exercise in reservoir engineering and can be found in Section 7.3 (keywords SGFN, SOF3 and SWFN).
Figure 20 represents reservoir fluids in equilibrium at initial conditions:

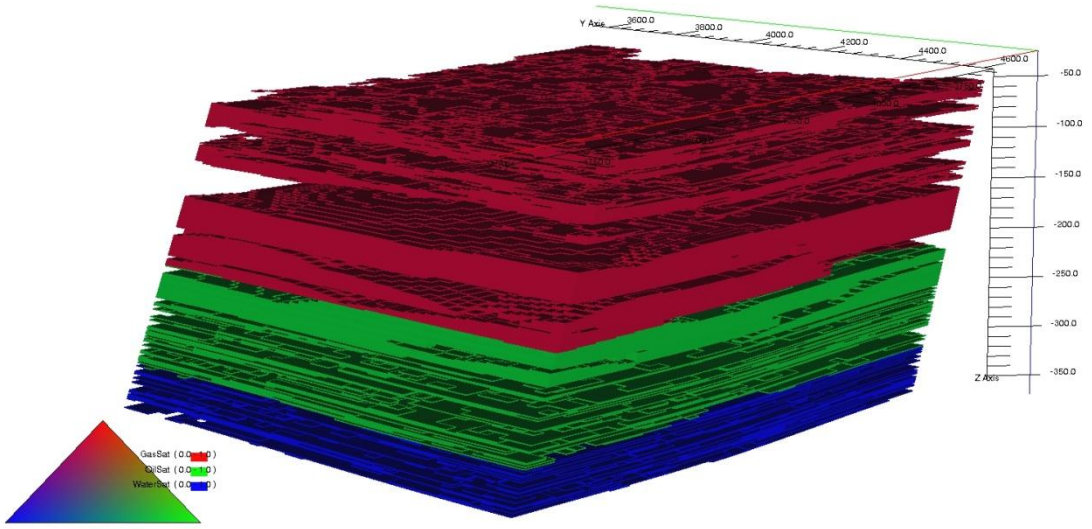

Figure 20: Initial fluids in equilibrium

After the model initialization, the fluids in place were calculated (Table 18).

Table 18: Fluids originally in place

Reservoir volume of oil	Reservoir volume of gas
13.044802×10^6 rm^3	18.457536×10^6 rm^3

3.3.3. Production Schedule

The main focus of this section is to devise a production strategy that enables the recovery of the greatest amount of oil possible while also dealing with the large amounts of gas produced.

Earlier it was shown (Section 3.2.3.3) that the gas produced in surface separators has a high content of CO_2. Also, in Table 5 of Section 3.2.2, it can be seen that both CO_2 and the C_2 fraction have very close critical temperatures[2]. For this reason, in this study, it is impossible to separate CO_2 from the remaining gas components using low pressure or cryogenic separators. This means that the produced dry gas cannot be sold and will have to be rejected. Resembling a field located 300km offshore, the production strategy will have to deal with the gas so that there is no need to export or flare it.

We first chose to approach the reservoir by producing the gas cap, to access the liquid condensate fraction of this volume. The fluid is condensed in surface separators and the resulting dry gas is rejected by re-injecting it back into the gas cap, to help keep reservoir pressure. The following Figure presents a simplified diagram of this production scheme:

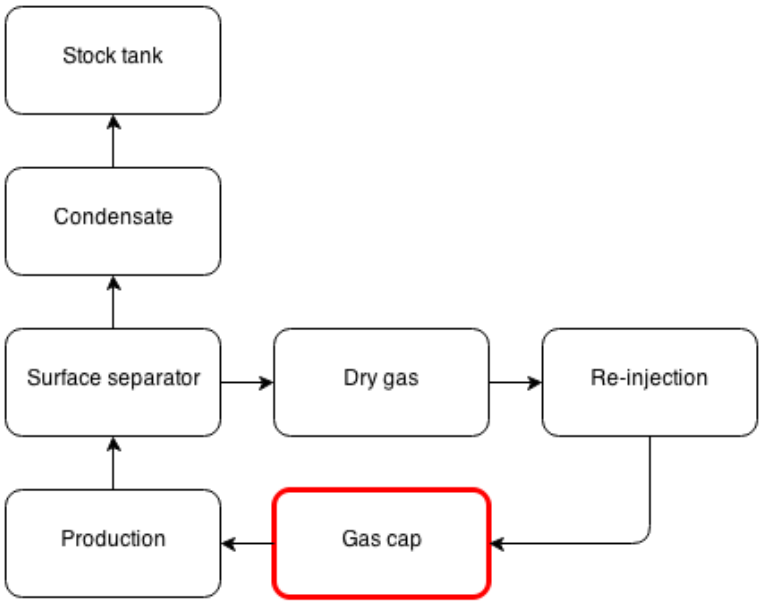

Figure 21: Production scheme for the gas cap

The well pattern chosen for this study was a traditional five-spot configuration with four vertical producer wells in the corners and one vertical injector well in the centre (Figure 22). Other configurations such as horizontal wells have been tried but performed poorly due to low vertical connectivity in the reservoir.

[2] Keep in mind that these parameters have been tuned to match the estimated observations and may not reproduce real fluid behaviour.

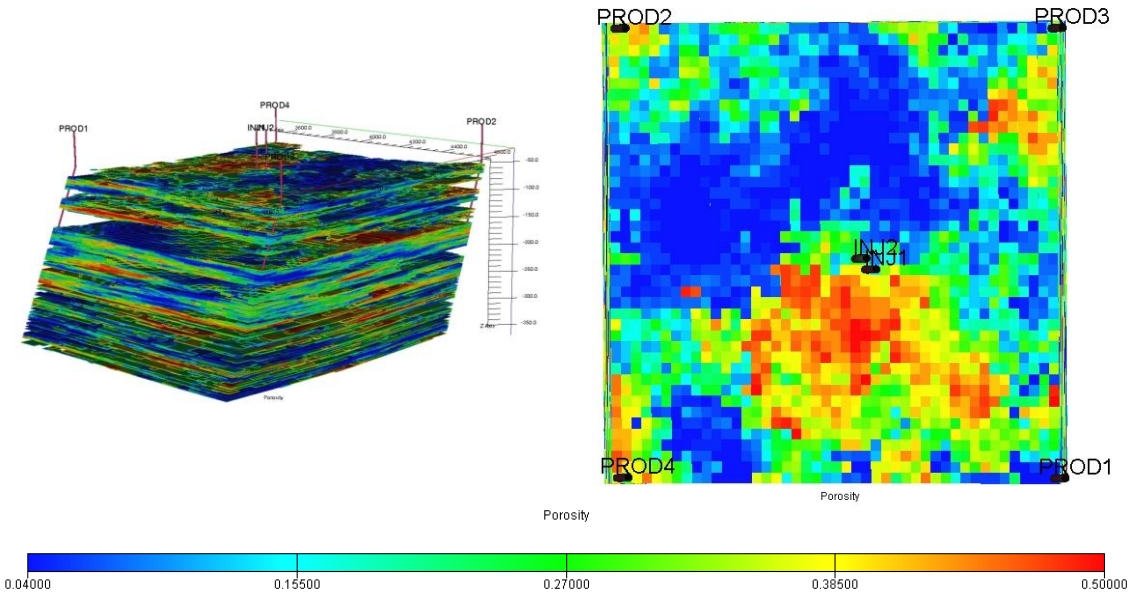

Figure 22: Well locations

The producer wells were set to a constant liquid flow rate of 150 sm^3/day, with a minimum working pressure of 350 bar. The gas re-injection well flow was tied directly to the gas production rate, so that the entire volume of gas produced was re-injected back into the reservoir (Table 19).

Table 19: Well completions and controls for the gas cap

Well	Top cell	Bottom cell	Flow (sm3/day)	BHP (bar)
PROD1	1	155	150	350
PROD2	1	155	150	350
PROD3	1	155	150	350
PROD4	1	155	150	350
INJ1	1	150	-	530[3]

The gas cap was produced for one year, after which the completions of the producer wells were closed in this zone and opened in the oil leg (Table 20).

Table 20: Well completions and controls for the oil leg

Well	Top cell	Bottom cell	Flow (sm3/day)	BHP (bar)
PROD1	170	250	150	350
PROD2	170	260	150	350
PROD3	170	250	150	350
PROD4	170	260	150	350
INJ1	1	150	-	530[3]
INJ2	170	300	-	500

As was shown in Section 3.2.3.4, the oil releases a large quantity of gas as soon as the pressure drops. To minimize this, a water injection well is required, to supply mass to the reservoir and to displace the oil. Figure 24 shows a simplified diagram of the production scheme for the oil leg:

[3] Gas re-injection pressure is limited by the minimum miscibility pressure defined in section 3.2.3.8

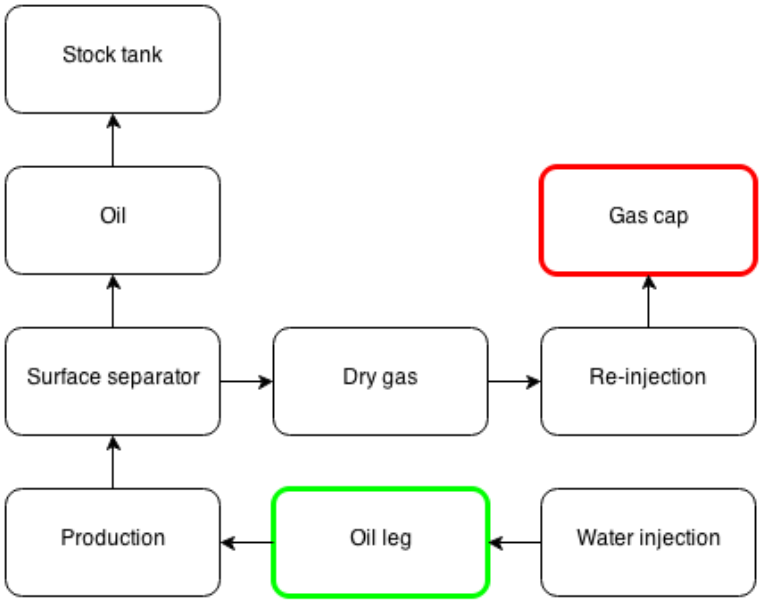

Figure 23: Production scheme for the oil leg

The same five-spot well pattern is used, with the addition of a sixth well for water injection, close to the gas re-injection well. As can be seen in the Figure above, the same gas re-injection strategy is applied, with all the gas liberated from the oil being re-injected back into the gas cap. Usually, water injection is only performed at a more advanced stage in the life of the reservoir but in this case it is started as soon as the oil leg is produced.

3.4. Production results

In this section, the reservoir production plots are presented and discussed, as well as the spatial evolution of the dynamic grid's properties.

We start with the field oil production rate and field water cut. From Figure 24, it is possible to obtain a stable nineteen year production plateau at 600 sm^3/day, after which there is a five year period with a very slow increase of the water cut. After the 24 stable producing years, a considerable water breakthrough starts to happen and production starts to decline. If we recall Section **3.3.3**, it was mentioned that the wells were limited to a water cut of 90%, with completions being closed on cells that exceeded this value. This can be seen by the oscillation in the declining production, corresponding to cell completions being closed, and the consequent temporary rise in the oil production rate.

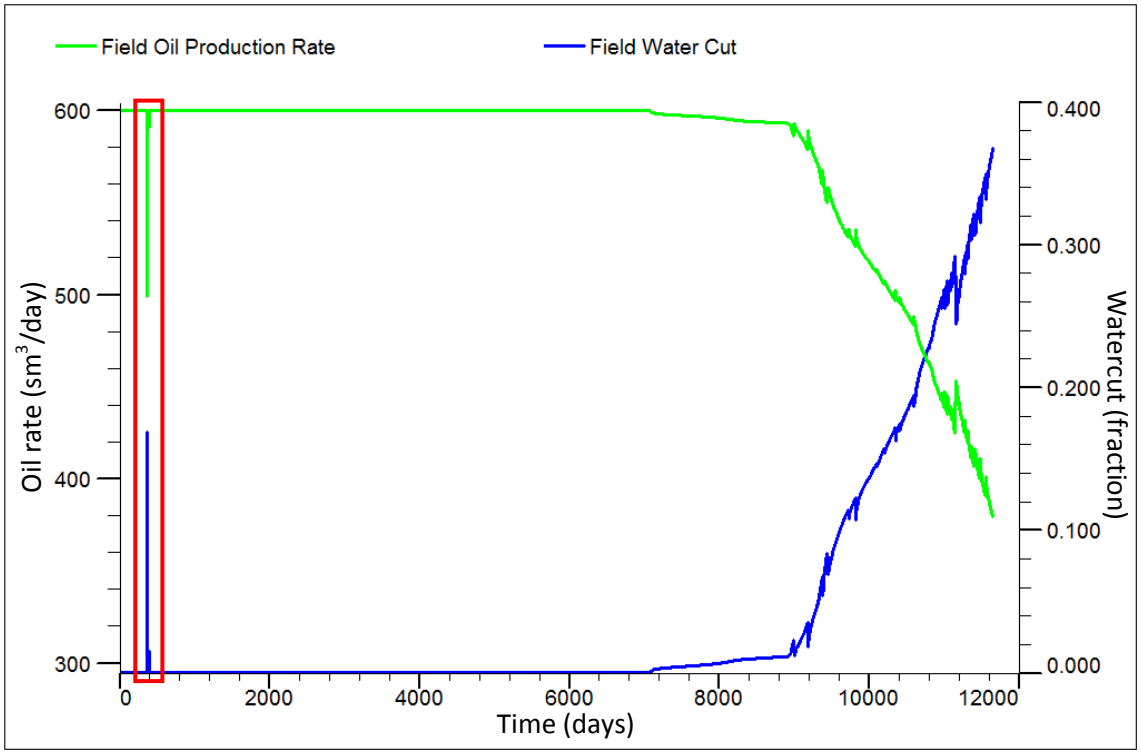

Figure 24: Oil production rate and water cut

One interesting aspect of the oil production rate and water cut is the spike that occurs at 365 days, outlined by the red box in Figure 24. It is actually caused by a pair of wells that are completed too deep and enter the aquifer, causing water to rise as soon as production starts in the oil leg.

At the end of the 32 year simulation period production dropped to just under 400 sm^3/day. Without any economic criteria regarding production costs it is not possible to forecast the expected field life but the reservoir shows an average decline rate of 24.3 sm^3/day per year.

From the initial 13.04 million rm^3 of oil, a total of 6.7 million sm^3 were produced during the simulated 32 years simulated (Figure 25).

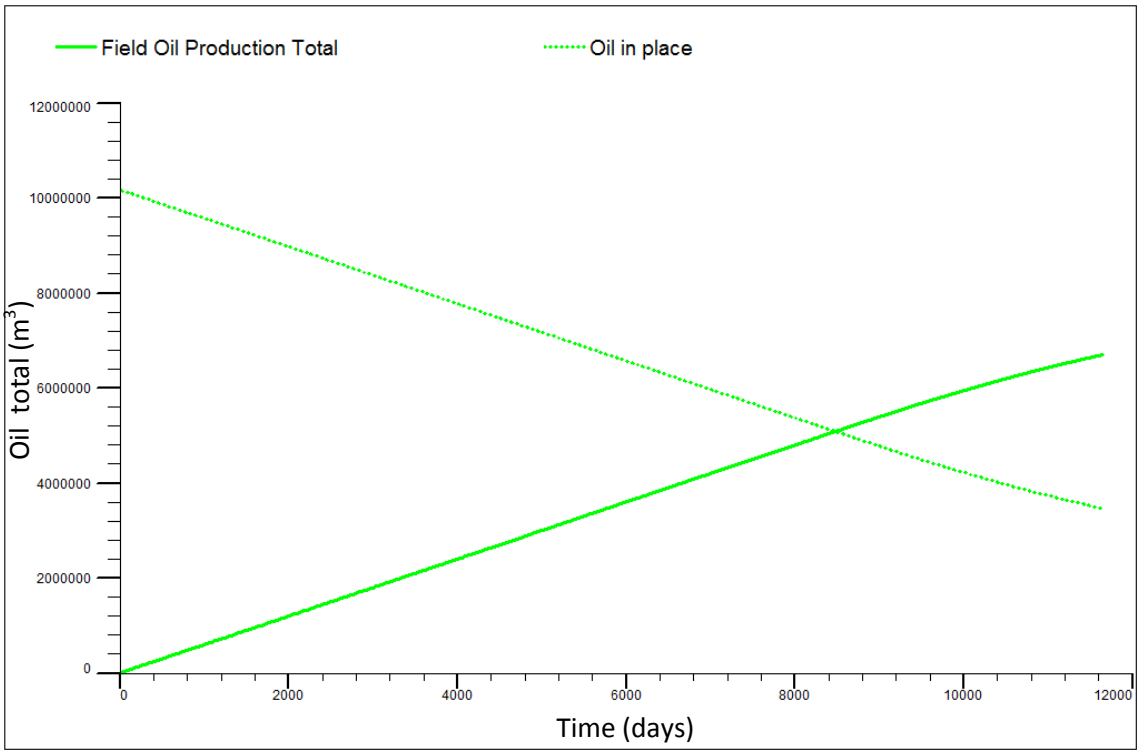

Figure 25: Total oil production and Oil in place

Another important parameter to be analysed in this specific field is the evolution of the gas cycling performance. Figure 26 contains both gas production and re-injection curves, as well as the total amount of gas produced and re-injected.

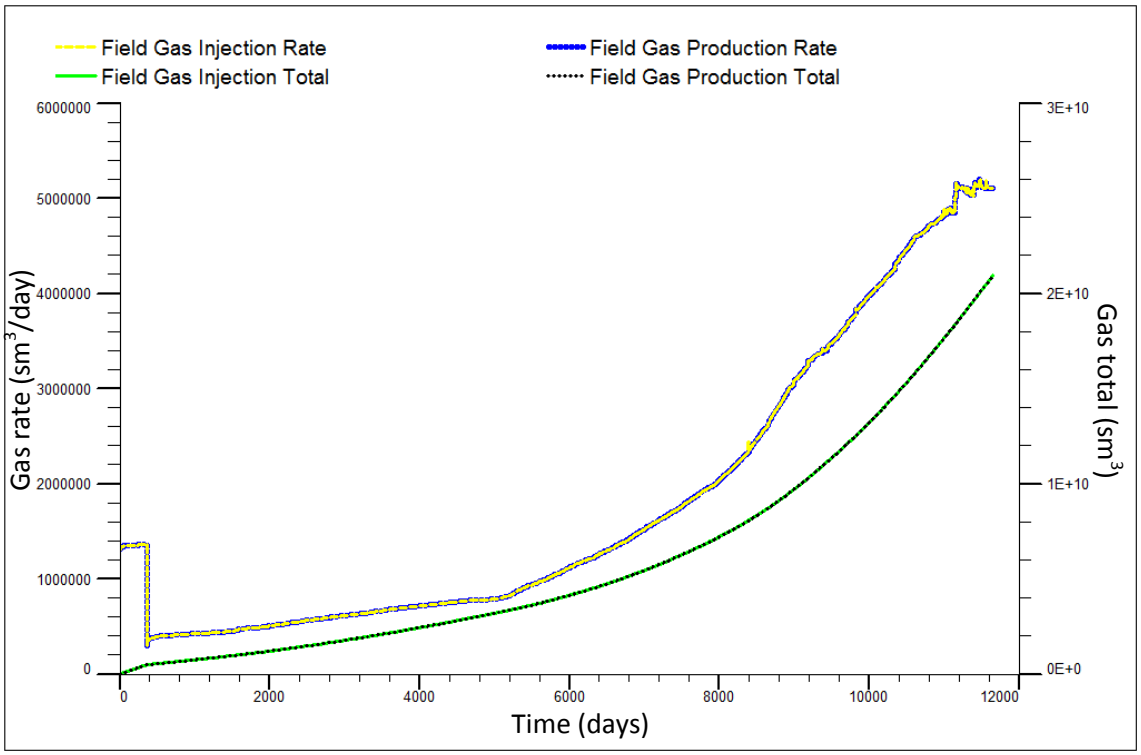

Figure 26: Field gas rates (upper) and gas totals (lower)

It becomes clear that the gas production and re-injection rates and totals are equal throughout the production of the field so it was possible to implement a complete gas cycling scheme parallel to the oil production, therefore eliminating the need to export it. This was one of the main objectives of the proposed production scheme. By the end of the simulation, the reservoir had produced 2.08×10^{10} sm3 of gas (twenty billion standard cubic meters)

Taking a closer look at the performance of each individual well, particularly their oil production rates, we can conclude that reservoir heterogeneities substantially influence the performance of wells (Figure 27).

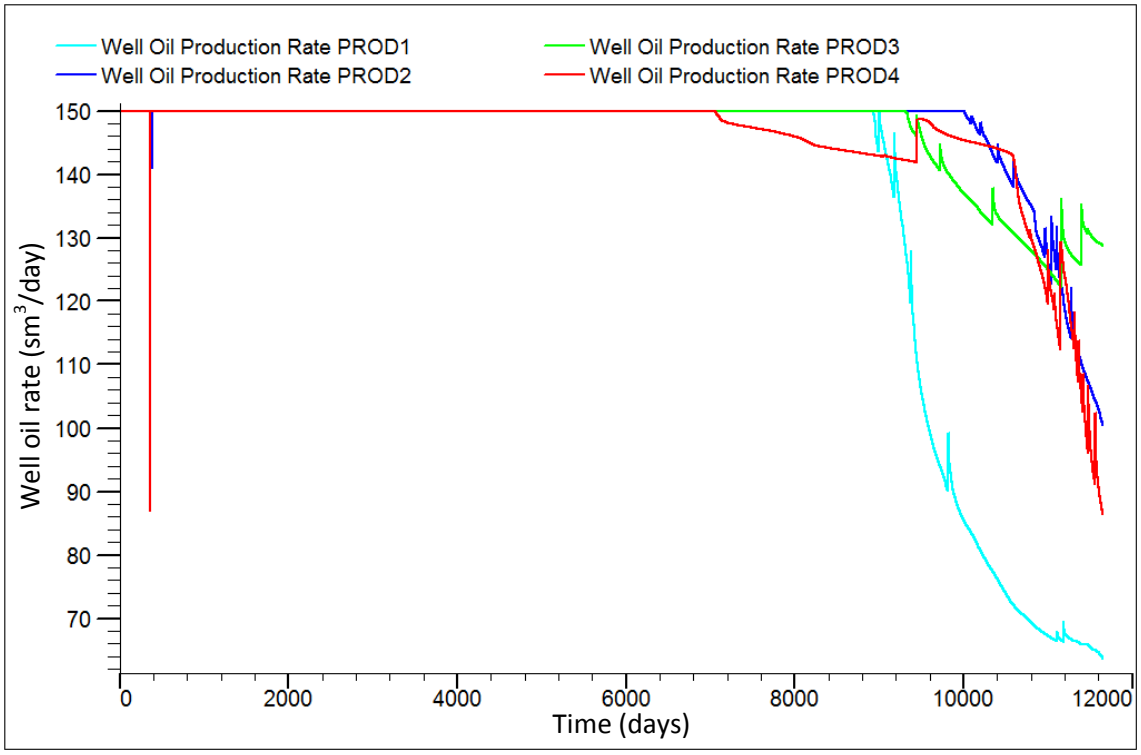

Figure 27: Well oil production rates

As mentioned previously, there is a drop in oil flow in wells PROD2 and PROD4 as soon as the oil leg starts production, due to water inflow from the aquifer. The PROD4 well is also the first to decline its production after nineteen years of production, causing the slight decline in field production mentioned earlier. Twenty four years into production the PROD1 well declines drastically, starting the decline in the overall field production as later wells PROD3 and PROD2 also decline.

As expected, if we observe the performance of each well in terms of water production (Figure 28) the exact complementary behaviour occurs: well PROD4 is the first to show water breakthrough at nineteen years of production; twenty four years into production well PROD1 shows a drastic water production increase, starting the decline of the oil production.

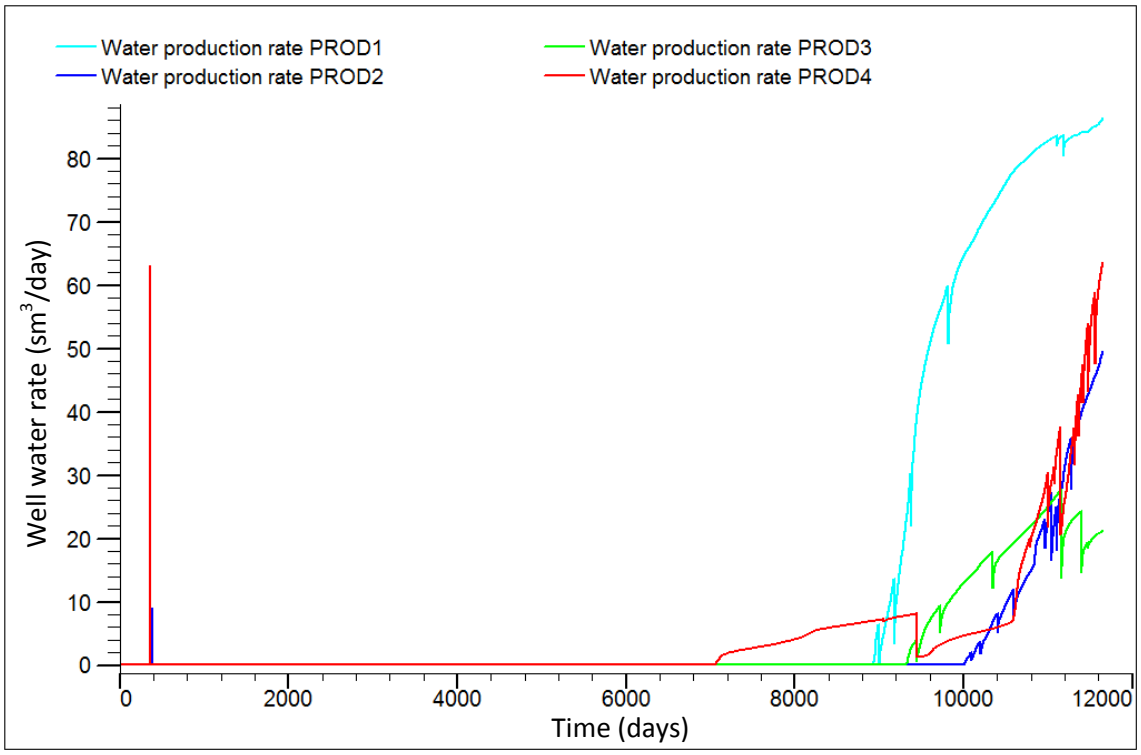

Figure 28: Well water production rates

Another important aspect in this analysis is the evolution of bottom hole pressures, as different wells evolve differently throughout the life of the field. In this run, bottom hole pressure is controlled and adjusted to a minimum of 350 bar to maintain a steady liquid flow of 150 sm^3/day. Due to the high heterogeneity of the reservoir, wells in different locations are exposed to different thicknesses of the formation and, therefore, have different areas exposed to flow. Recalling that fluid flow is dependent on the flow area and also the pressure gradient, it is obvious that wells with less area of exposure will require a greater drawdown to keep up with the flow requirements.

Figure 29 contains the evolution of the bottom hole pressures for the four producer wells. It is evident that each well has a distinct behaviour, having different changes in pressure over time. One interesting detail in this evolution is that there is a clear difference between the gas cap and the oil leg production. The well PROD3, for instance, required the highest pressure drop to produce the desired flow in the gas cap, while on the oil leg it was the opposite. We can also see that this well has a very constant bottom hole pressure throughout the production, whilst the other three present significant changes.

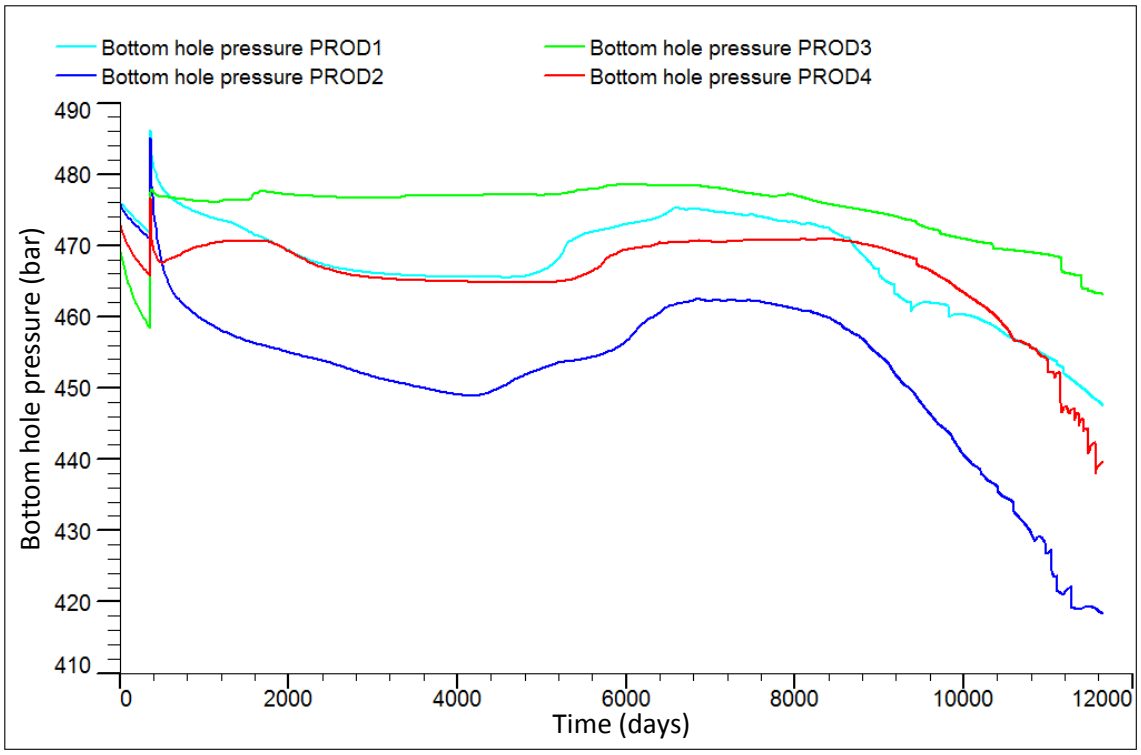

Figure 29: Well bottom hole pressures

In terms of average field pressure (Figure 30) it can be seen that this production scheme allowed the field to be produced with a small average pressure drop.

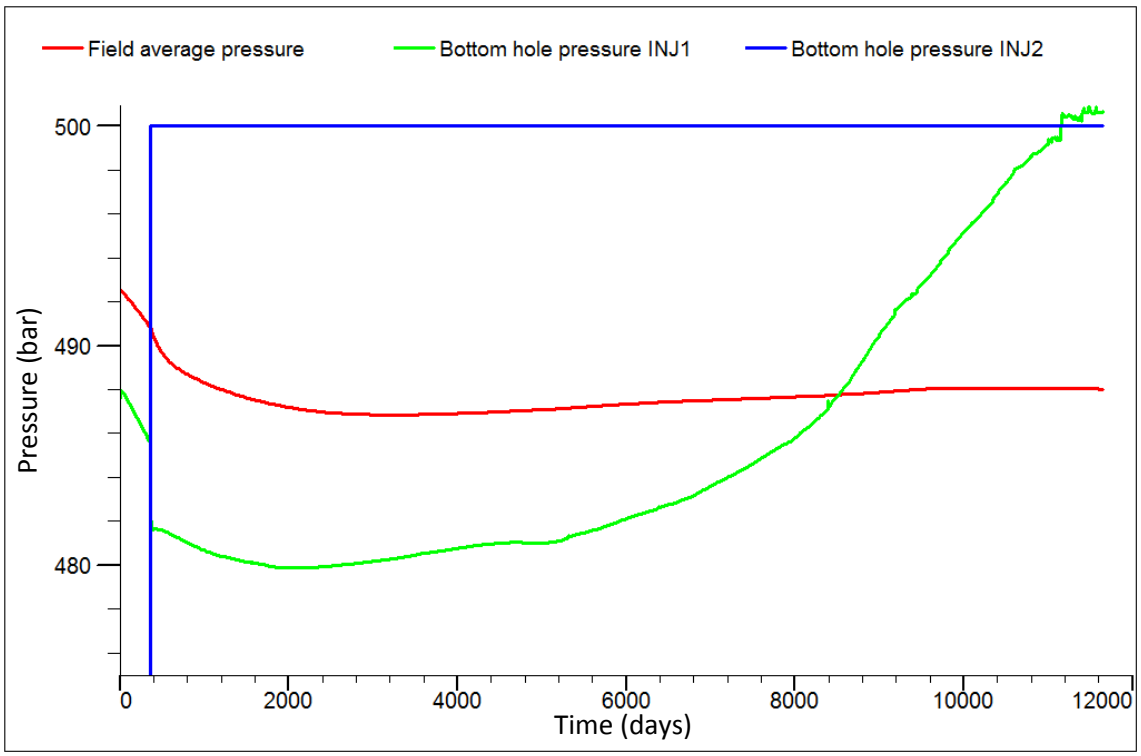

Figure 30: Evolution of average reservoir pressure and injection pressures

Regarding injection pressures we see that the injector INJ2 has a constant water injection pressure, as defined in the simulation, while the gas re-injection pressure in well INJ1 continuously rises. This is due

to the fact that the gas-reinjection well is continuously injecting large volumes of gas into the gas cap and requiring ever increasing pressures to compress it.

Observing the evolution of the dynamic properties within the reservoir grid (Figure 31), it is possible to detect asymmetries in the evolution of the water displacement front, caused by heterogeneities in the reservoir.

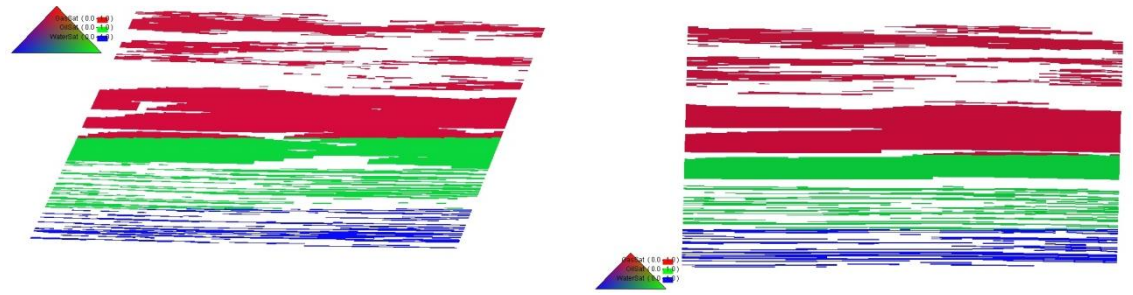

01 January 2014

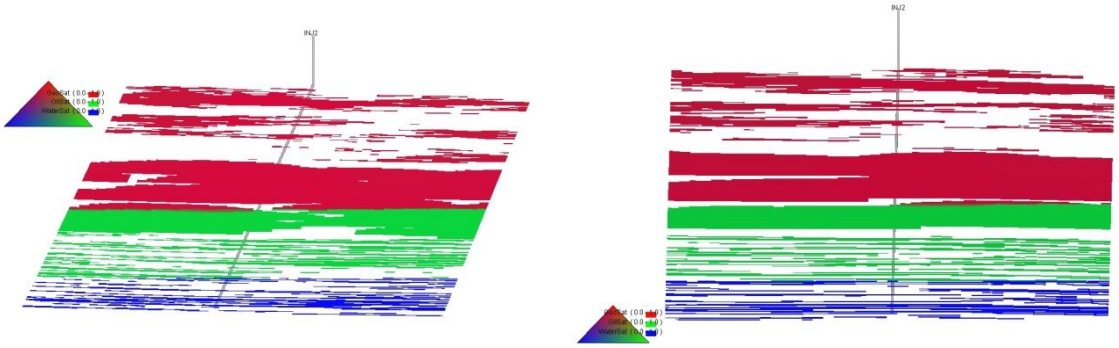

01 January 2015

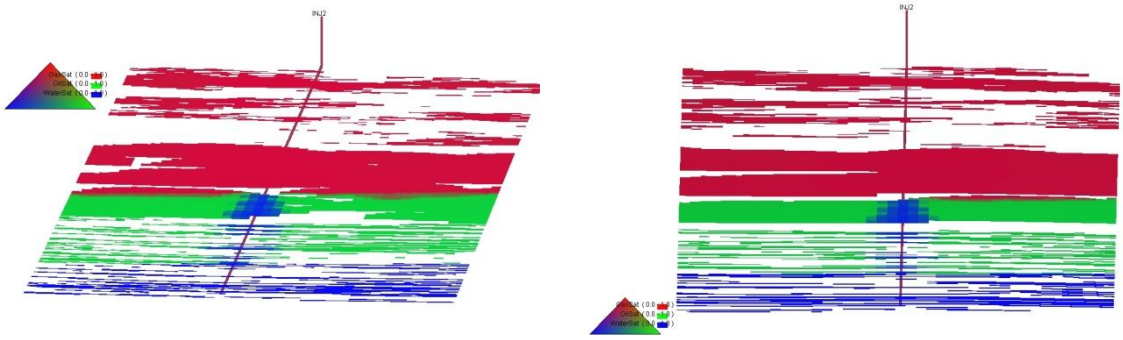

01 January 2016

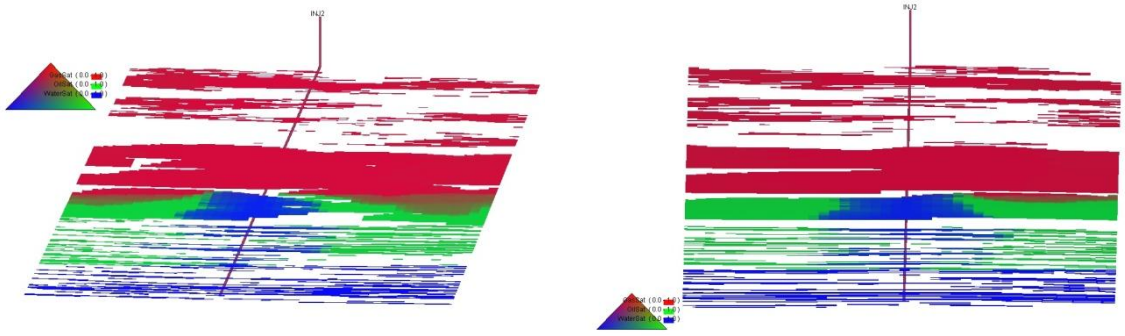

01 May 2020

Oil Gas water

Figure 31: Ternary grid in slice i=20 (left) and j=20 (right)

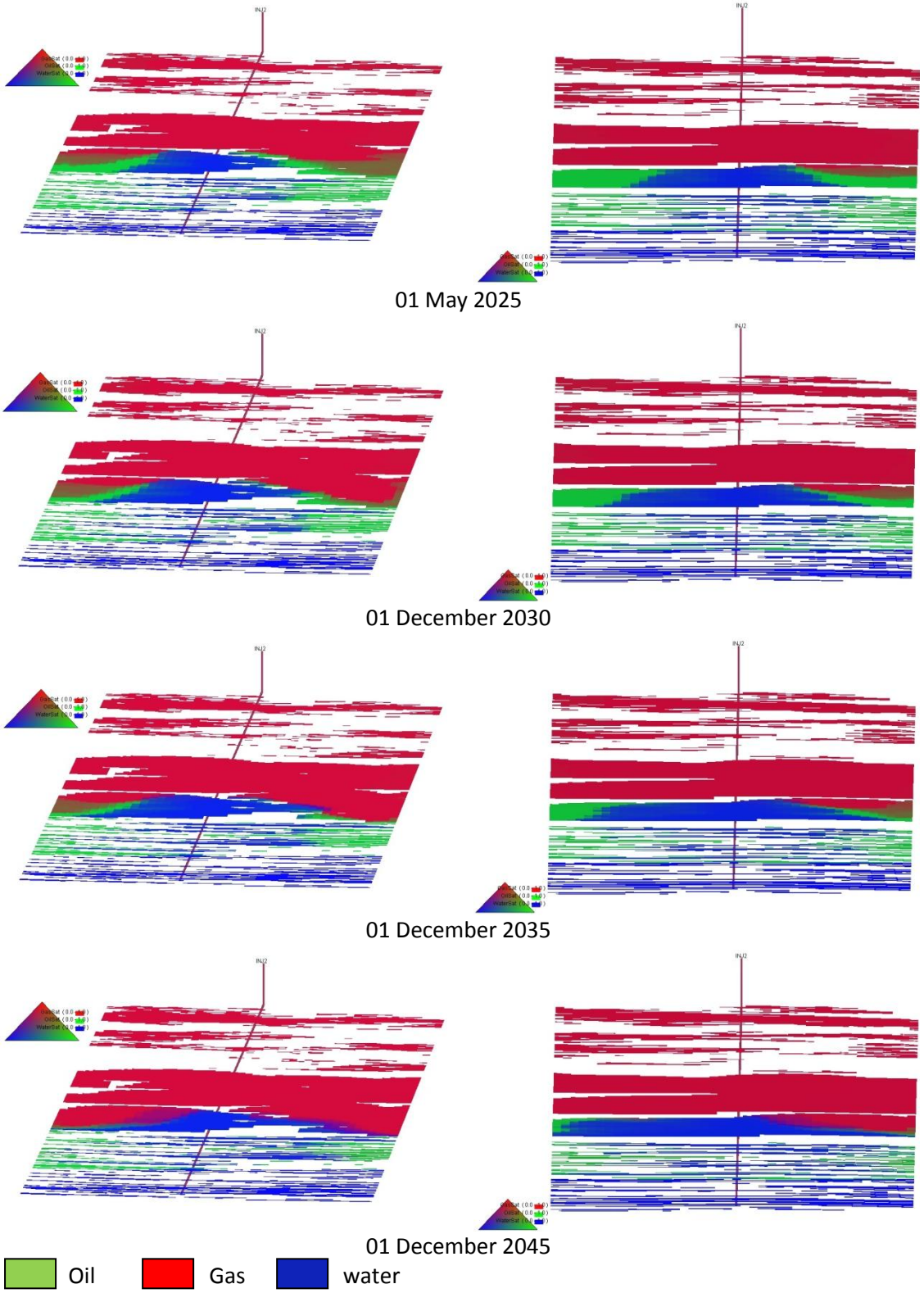

Figure 31 (continued): Ternary grid in slice i=20 (left) and j=20 (right)

By the end of 2045 the top of the oil leg has been swept fairly efficiently while the lower part of the reservoir still shows oil pockets, showing the influence of reservoir heterogeneities and poor connectivity. Another aspect that draws attention is the gas cap weighting down on the oil leg towards the end of production, manifested by the lowering of the gas-oil contact. This is caused by the constant

addition of mass to the gas cap, with the corresponding pressure build-up, whilst the oil leg is under a pressure drawdown.

Tables 21 and 23 gather the total fluids produced by the reservoir:

Table 21: Total fluids produced and injected (metric units)

	Gas cap	Oil leg
Total oil produced (sm^3)	$2.16x10^5$	$6.48x10^6$
Total gas produced (sm^3)	$4.95x10^8$	$2.04x10^{10}$
Total gas re-injected (sm^3)	$4.95x10^8$	$2.04x10^{10}$
Total water produced (sm^3)	1.35	$2.9x10^5$
Total water injected (sm^3)	-	$4.63x10^6$

Table 22: Total fluids produced and injected (field units)

	Gas cap	Oil leg
Total oil produced (bbl)	$1.36x10^6$	$4.07x10^7$
Total gas produced (scf)	$1.74x10^{10}$	$7.2x10^{11}$
Total gas re-injected (scf)	$1.74x10^{10}$	$7.2x10^{11}$
Total water produced (bbl)	8.49	$1.82x10^6$
Total water injected (bbl)	-	$2.91x10^7$

4. Seismic monitoring

This section of the thesis explores some advantages of the compositional fluid flow simulation to model the changes in the seismic response of the reservoir during production. This step aims to mimic real reservoir monitoring during production. Once the flow simulation was run and optimized, the data regarding fluid saturation, density and compressibility from simulated time steps was gathered.

A rock physics model was created for these specific time steps using the Xu-Payne methodology (Xu & Payne, 2009) and a set of synthetic time-lapse seismic data was then computed using a convolutional forward model for each selected time step. The changes in seismic response were observed by subtracting the seismic volumes. The Shuey's approximation of the Zoeppritz equations was used to compute the angle-dependent synthetic reflection coefficients allowing simultaneously an AVO analysis on each time step. For a better observation of the influence of pore fluids on the seismic response of the reservoir, seismic attributes such as the Lamé parameters were calculated and revealed distinct trends for each fluid type.

4.1. Rock physics model

The first step towards the generation of seismic data was to create a rock physics model which reproduced the model's elastic parameters as a function of porosity. The mineral matrix elastic properties were modelled using the Voigt-Reuss-Hill average of the minerals present. We used, for the reservoir facies, the Lagoa Salgada's stromatolites (Archilha, Missagia, Ceia, & Neto, 2013) composition. Its mineral proportions and properties in Table 23.

Table 23: Mineral percentages and elastic moduli for the reservoir facies

Mineral	Percentage	K(GPa)	μ(GPa)
Calcite	85%	76.8	32
Quartz	10%	37	44
Aragonite	5%	44.8	38.8

The Mudstone facies was assumed to be exclusively composed by Calcite. Table 24 contains the mineral matrix properties for both facies.

Table 24: Elastic moduli for both facies

Facies	K(GPa)	μ(GPa)
Reservoir	69.198	33.368
Mudstones	76.8	32

Following the methodology proposed by Xu&Payne (Xu & Payne, 2009), the rock's porosity was divided in two types: closed micro pores and connected macro pores. In this methodology, the closed micro pores are treated as inclusions in the rock matrix, and modelled with the Differential Effective Medium

theory. Without any data to model the closed porosity it was simply assumed as being 5% of the total porosity for both facies. Figure 32 shows the elastic moduli as a function of the closed porosity.

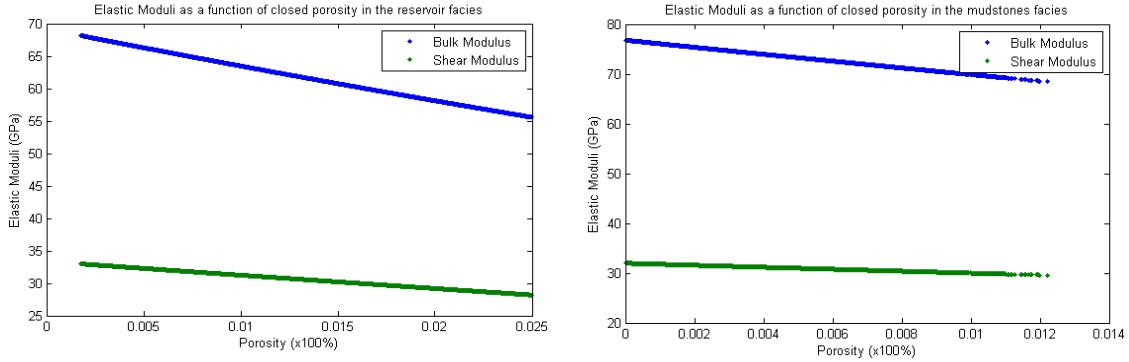

Figure 32: Elastic Moduli as a function of closed porosity

At this stage we now have an elastic model of the mineral matrix with enclosed micro pores. Not having enough real data to produce a rock physics model based on contact theories, on which carbonates are seen as granular media with clastic-like morphology parameters such as number of grain contacts or critical porosity, a simpler approach was taken and a Hashin-Shtrikman theoretical bounds model was calculated. Figure 33 contains the resulting elastic moduli for both facies.

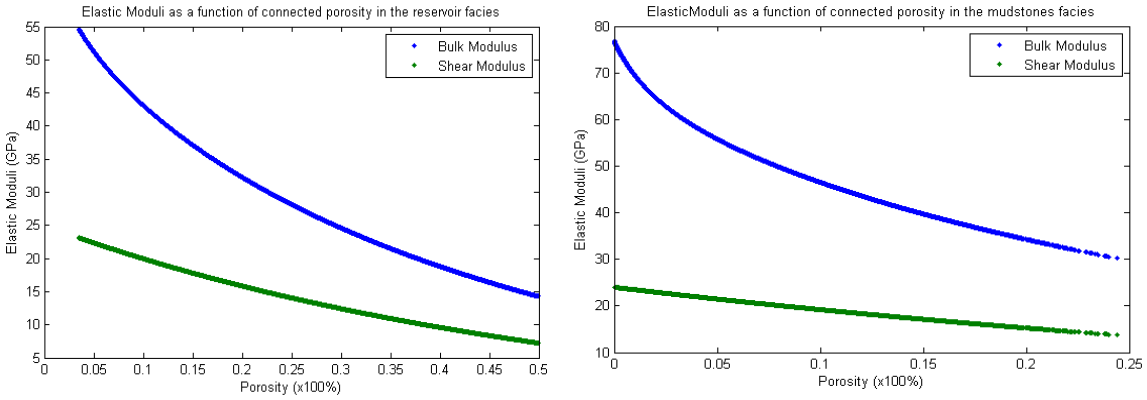

Figure 33: Elastic Moduli as a function of connected porosity

Having a dry rock elastic model, the next step is to fill the connected pore space with the fluids simulated in the dynamic modelling. This was done using Gassmann's fluid substitution (Smith, Sondergeld, & Rai, 2003), which relates the Bulk modulus of the rock saturated with a fluid with the Bulk modulus of the fluid itself, the dry rock's Bulk modulus, the mineral matrix Bulk modulus and the porosity.

Usually the Gassmann's substitution is accompanied by another technique known as the Batzle-Wang relation (Batzle & Wang, 1992), which allows an estimation of the fluid Bulk modulus as a function of reservoir conditions and fluid properties. Since this section of the work is based on the results obtained with the compositional simulation (which uses a much more sophisticated equation of state when

compared to the Batzle-Wang technique) there is no need to use this, as it is possible to obtain the pore fluid compressibility directly as a simulation output. Since the Bulk modulus of a substance is equal to the inverse of its compressibility (Mavko, Mukerji, & Dvorkin, 2009) it is rather simple to obtain it.

Seven simulated time steps were chosen and the Bulk modulus of the pore fluid was calculated, for every cell. The chosen time steps are listed below in table 25.

Table 25: Selected time steps for the seismic monitoring

Step zero	01-January-2014
Step one	01-January-2015
Step two	01-January-2021
Step three	01-December-2027
Step four	01-December-2033
Step five	01-December-2039
Step six	01-December-2045

Step zero corresponds to the initial conditions, to which all data will then be compared. Step one corresponds to the end of the gas cap production, and the beginning of water injection in the oil leg. As the production strategy remains the same through the remaining reservoir life, equally spaced steps were chosen up to the point where reservoir production declines.

Since fluid flow was not simulated in the Mudstones facies, the pore space in this facies was only filled with brine. As for the reservoir facies, the fluid substitution was performed for each time step, resulting in seven distinct models of reservoir Bulk modulus. The model of **μ** remains constant throughout the simulation, as the fluid shear modulus is always null. The next Figure contains a comparison of histograms of pore fluid Bulk modulus for the initial equilibrium conditions and the end of the simulation:

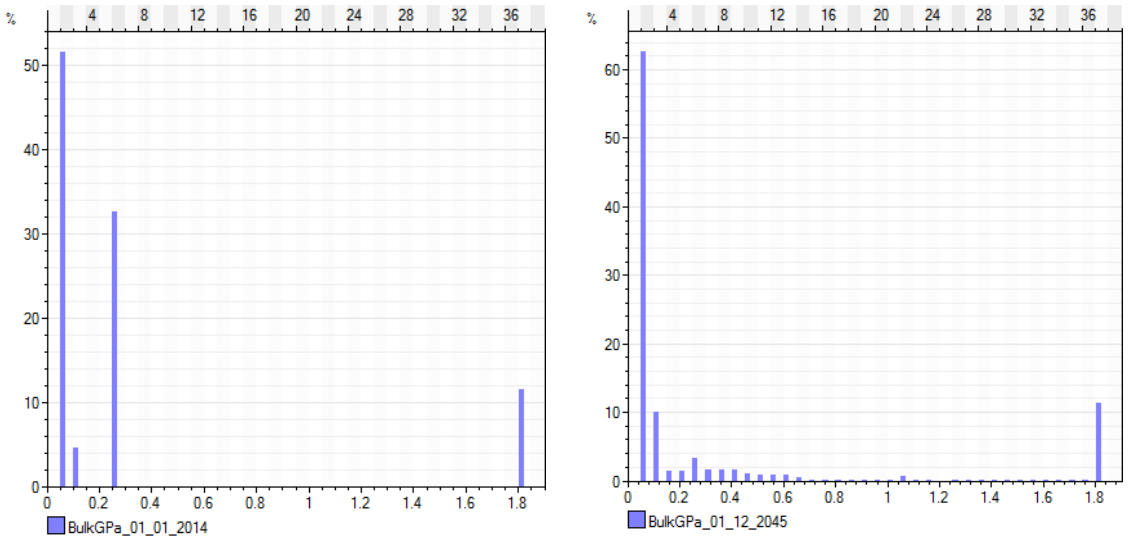

Pore fluid Bulk modulus for 2014 (GPa) Pore fluid Bulk modulus for 2045 (GPa)

Figure 34: Histograms of pore fluid Bulk modulus

The compositional fluid flow simulation also allowed an accurate description of pore fluid densities, as values of fluid densities and saturations can be obtained for each cell.

Having composed models of elastic moduli and density for each selected time step it was possible to compute seismic velocities for each cell.

The result is a volume of seismic velocities and densities for each selected time step, which can now be used to compute synthetic seismic.

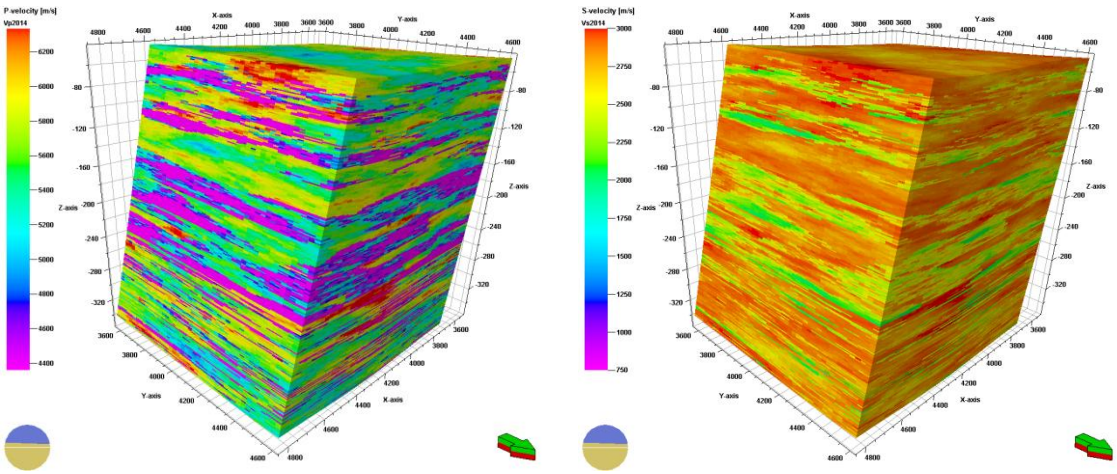

Figure 35: P-wave (left) and S-wave (right) velocity models used to compute the seismic models for the initial conditions

4.2. Synthetic seismic volumes

The Shuey approximation of the Zoeppritz equations (Avseth, Mukerji, & Mavko, 2005) was used to calculate the reflection coefficients for twenty five angles of incidence (from 0 to 45 degrees). For each offset angle, an angle-dependent wavelet was provided and, using a convolutional forward model, seismic amplitudes were calculated for each cell. Figure 36 contains the wavelets used to compute the time-lapse seismic data from the elastic models calculated from the compositional fluid flow simulation.

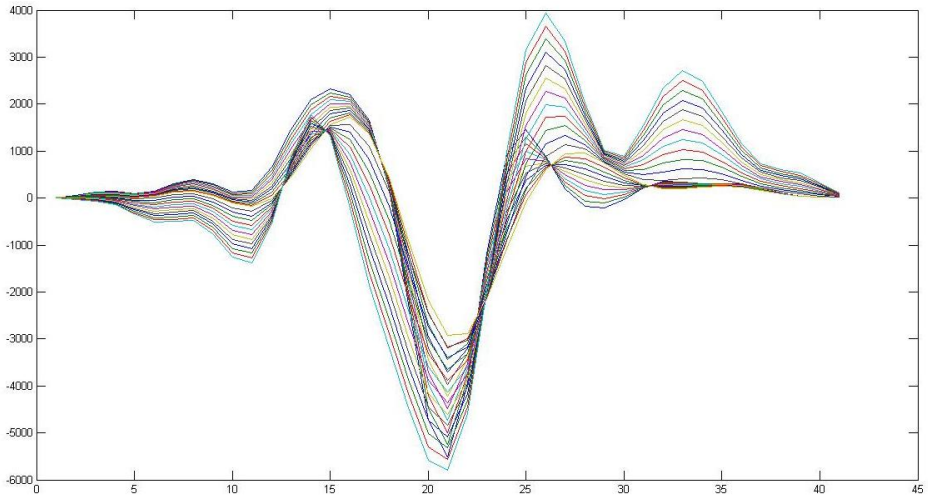

Figure 36: Angle-dependent wavelets used for the convolution

The seismic volumes were then divided in three groups and stacked: a near-stack, with offsets from 0^{o} to 16.2^{o}; a mid-stack, with offsets from 14.4^{o} to 30.6^{o}; and a far-stack, with offsets from 28.8^{o} to 45^{o}. A full-stack volume was also created as an average of all offsets.

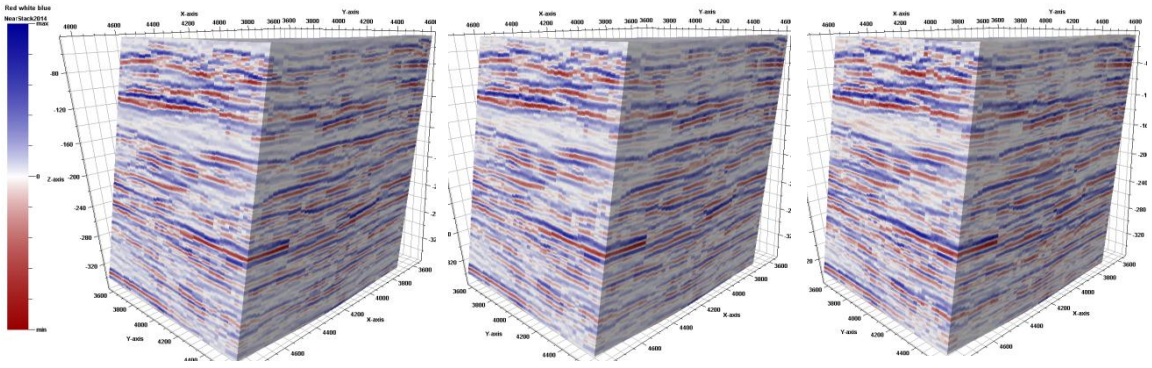

Near stack **Mid stack** **Far stack**

Figure 37: Partial stack seismic volumes for the initial conditions

Large offset reflections are more influenced by contrasts in pore fluid density (Avseth, Mukerji, & Mavko, 2005). For this reason the far-stacks were used to calculate volumes of differences in amplitudes, between the initial seismic and the remaining volumes along the selected time steps. Figure 38 shows the differences in amplitudes between each selected time step and the original conditions.

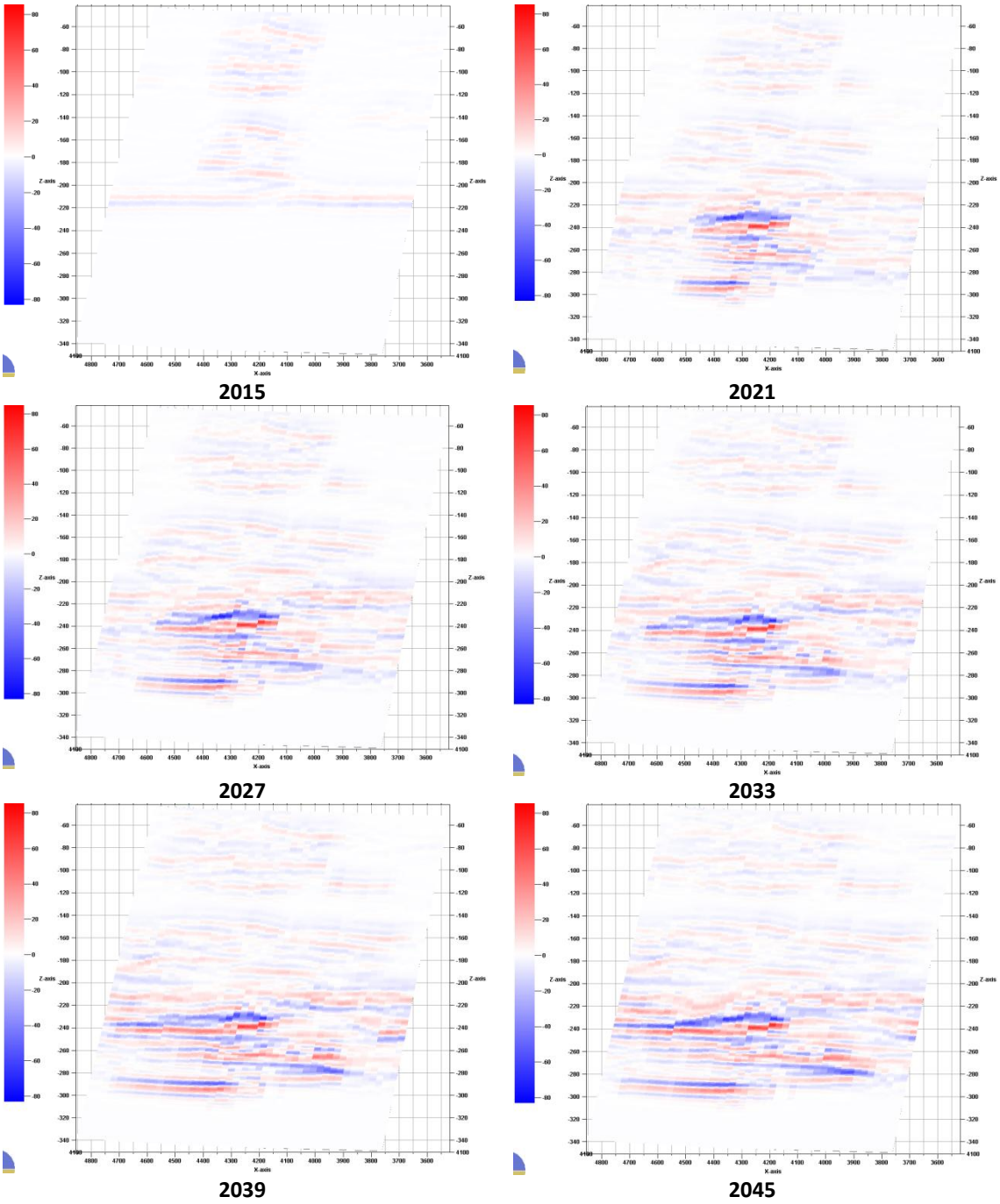

Figure 38: Differences in seismic amplitudes relative to the initial seismic volume, in section i=20.

If we recall the production scheme discussed in section 3.3.3 it was mentioned that the gas cap was produced for one year, followed by the oil leg production, with water being injected in it from the beginning. Comparing the evolution of water saturations obtained from the dynamic simulator with the

corresponding differences in the seismic response of the model (Figure 39) produces interesting results that may be an added value for seismic reservoir monitoring.

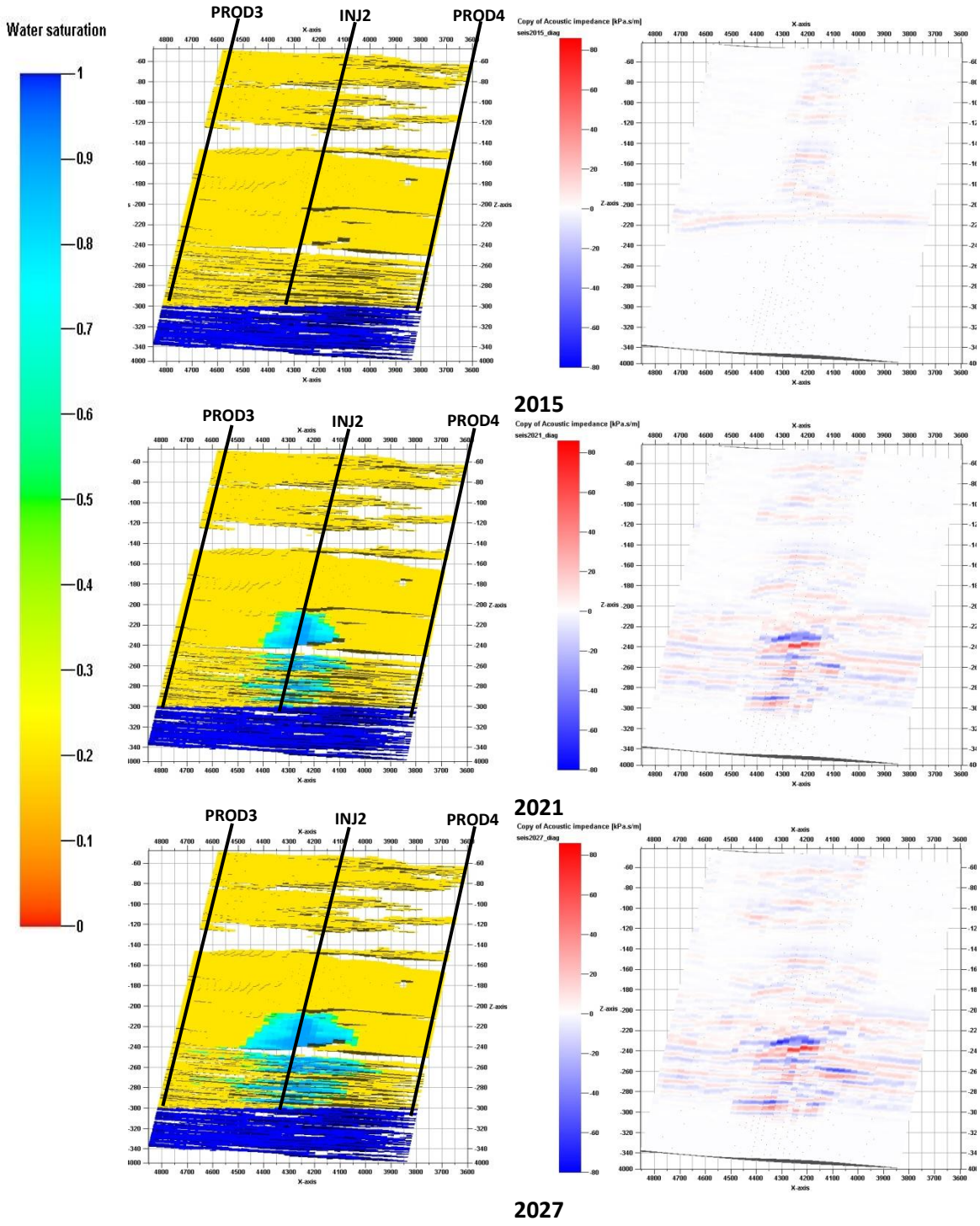

Figure 39: Evolution of Sw (left) on a diagonal cross section and its effects on the seismic response (right)

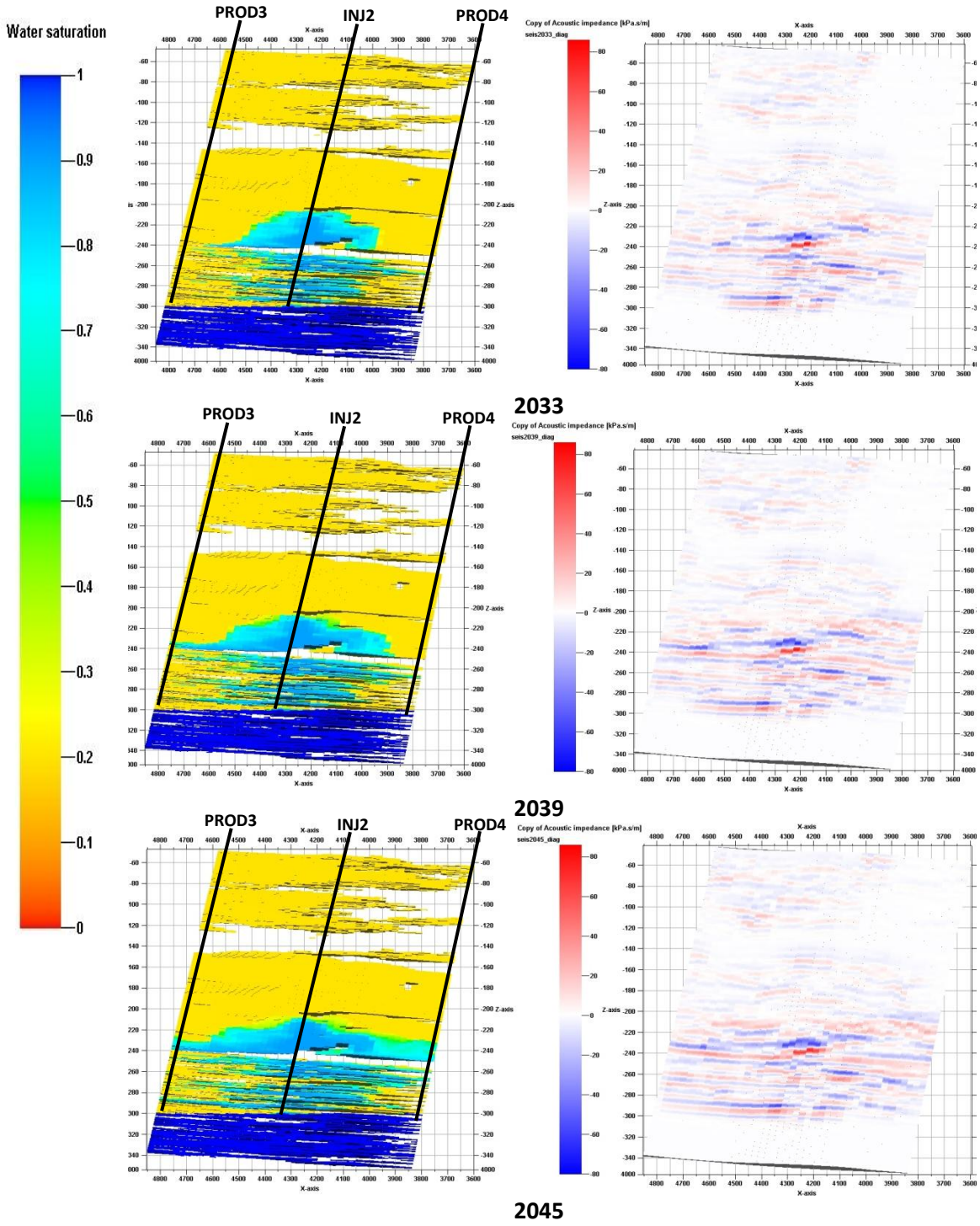

Figure 39 (continued): Evolution of Sw (left) on a diagonal cross section and its effects on the seismic response (right)

It becomes clear that the water injected in the oil leg strongly affects the seismic response of the rock, since water has a significantly lower compressibility when compared with the oil. This effect results in a good correlation between the water injection and strong seismic reflections.

To access the magnitude of changes in seismic amplitudes, the seismic volumes were divided by the initial volume. Figure 42 shows an example of a normalized histogram for changes in seismic amplitudes from 2014 to 2027.

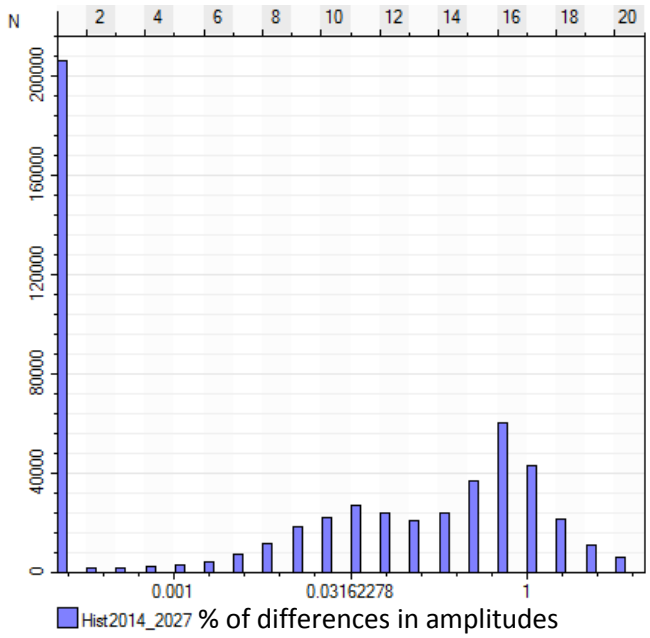

Figure 40: Histogram of amplitude differences from 2014 to 2027

It can be seen that most changes in seismic amplitudes from 2014 to 2027 occur up to 1%, with few changes reaching 10% or higher. This was expected since the highest contrast in Bulk modulus within the reservoir is 1.77 GPa, corresponding to the difference between the aquifer and the most compressible gas at the top of the gas cap. Since none of these two fluids is replaced by the other during production, the changes in pore fluid Bulk modulus are lower and, therefore, the small changes observed in the seismic amplitudes are as expected.

4.3. AVO analysis

Carbonate reservoirs are notorious for not giving away their secrets in AVO analysis, as this theory was originally developed for gas sands with shale seals (Castagna, 1993). These reservoirs are sometimes sealed by the same type of rocks with lower porosity. These differences cause Rutherford & Williams AVO classes (Mavko, Mukerji, & Dvorkin, 2009) to not apply to these cases. Nevertheless, an AVO analysis was performed on this model. Figure 43 shows a gather of pre stack seismic traces for all offsets on cell I=20, J=20:

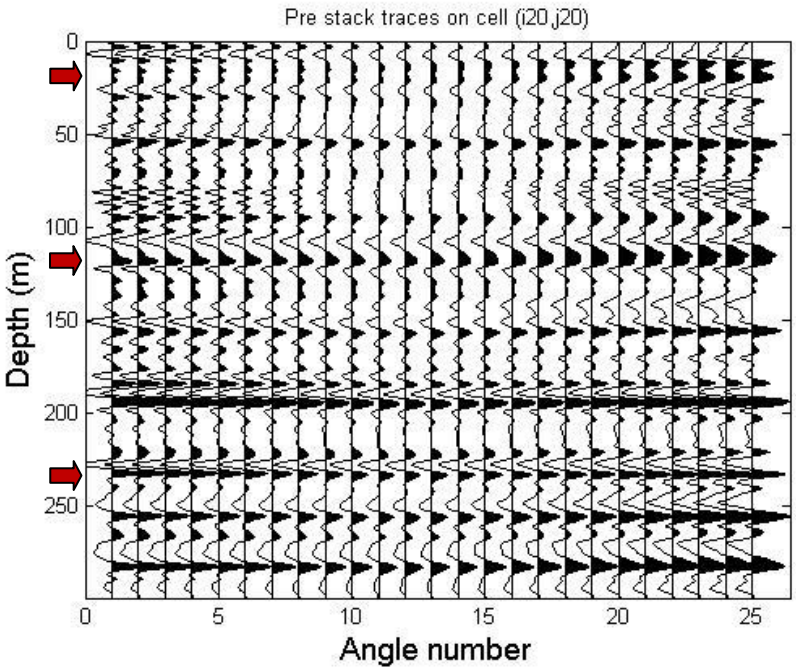

Figure 41: Pre stack seismic traces on cell I=20, J=20, for the initial conditions

In the pre stack seismic traces it can be seen that at some depths the amplitude of reflections increases with the offset angle, as indicated by the red arrows.

The AVO plots (Figure 44) allow the identification of the interfaces between sealant facies and hydrocarbon bearing rocks, as these are usually reflectors with negative reflection coefficients at normal incidence (Intercept or R_0) and exhibit positive gradient values (amplitudes increase with offset).

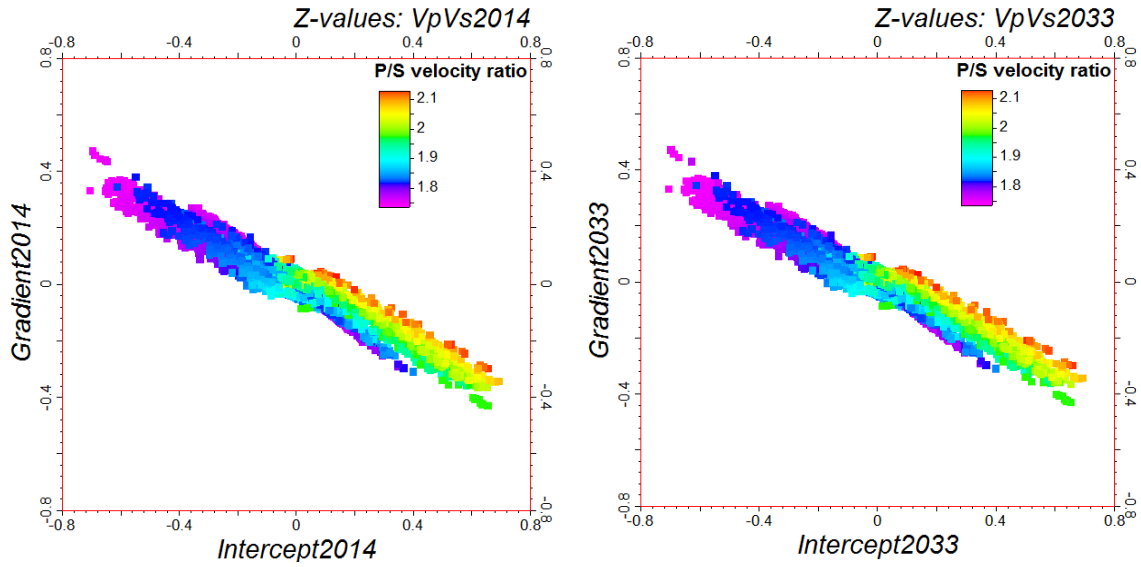

Figure 42: AVO plot for 2014 (left) and for 2033 (right)

Although some separation of AVO trends can be identified, with reservoir fluids occupying the upper left quadrant, this does not prove to be of any significant value to the seismic monitoring of the reservoir, as little or no changes occur in AVO behaviour over time.

4.4. Seismic attributes

For a better distinction of the seismic response of reservoir rocks containing different fluids, some seismic attributes such as the Lamé parameters were calculated and analyzed.

$$\mu = \rho Vs^2$$ **Equation 19: μ Lamé parameter**

$$\lambda = \rho Vp^2 - 2Vs^2$$ **Equation 20: λ Lamé parameter**

From the plot of **μ** as a function of **λ** (Figure 43) it can be seen that there are three distinct trends of Lamé parameters: the Mudstones trend, reaching higher **λ** values with a narrower **μ** window; and two similar trends with a wider range of **μ** values. These two trends correspond to the aquifer trend (on the right) and the hydrocarbons trend (on the left). Taking a closer look it becomes clear that the hydrocarbons trend actually corresponds to another two very close trends: one on the left corresponding to the gas trend; and one on the right which corresponds to the oil trend.

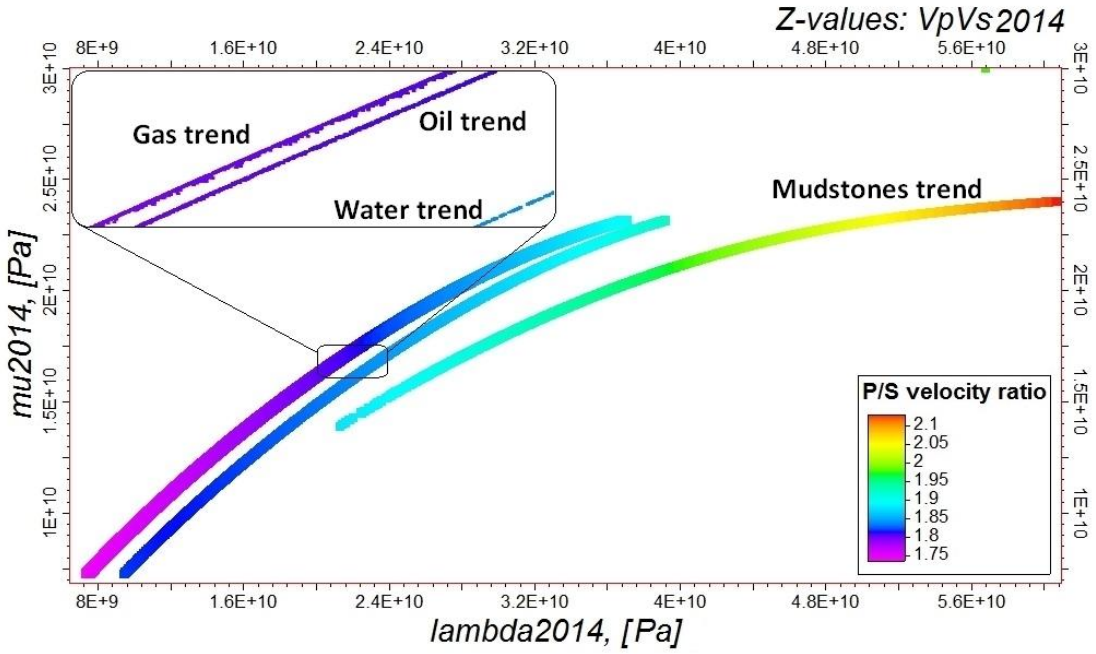

Figure 43: Seismic attribute trends for the initial conditions (2014)

The next step was to observe if there were changes in these trends as time moved forward and the reservoir was produced. The first time lapse corresponds to the production of condensate from the gas cap, involving only the production of fluid at producer wells and re-injection of gas in an injector well.

Figure 44 shows that some cells have moved from either the gas or oil trend and now have an intermediate behaviour. Applying an inclusive filter for these cells on the seismic volume of 2015 it shows that these cells broadly correspond to the gas-oil contact.

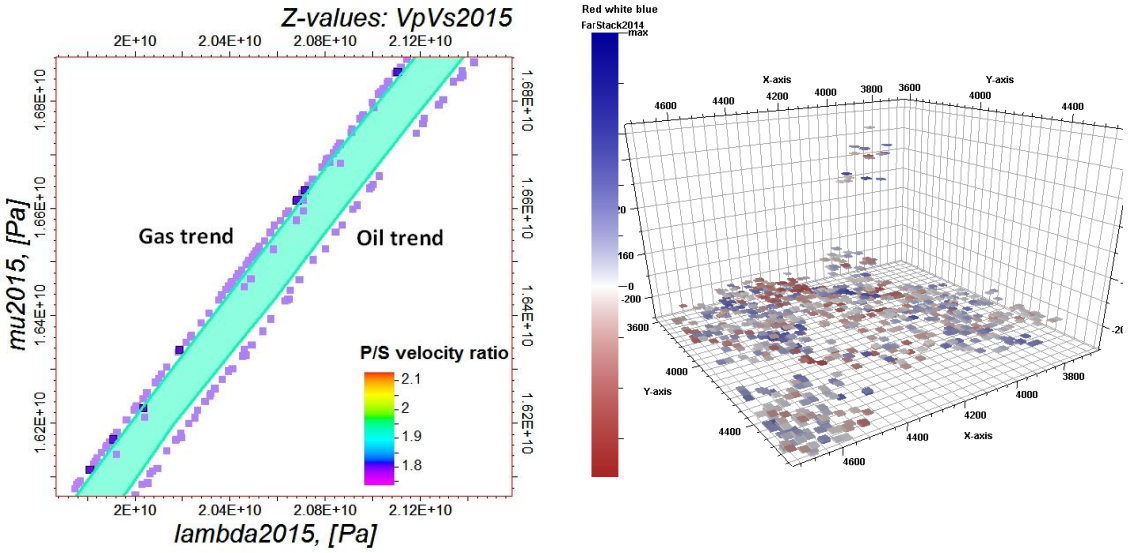

Figure 44: Intermediate gas-oil trend filter (left) and corresponding seismic cells (right)

Calculating volumes of differences in seismic attributes it becomes clear that the migration of cells from one trend to another is not as straightforward as it appeared. As can be seen in Figure 45, the cells that present an increase in **λ** correspond to the surroundings of the gas re-injection well, where gas is compressed and acquires a stiffer seismic response, and also to the producer wells on the corners, where the liquid condensation due to the production drawdown induces a stiffer response.

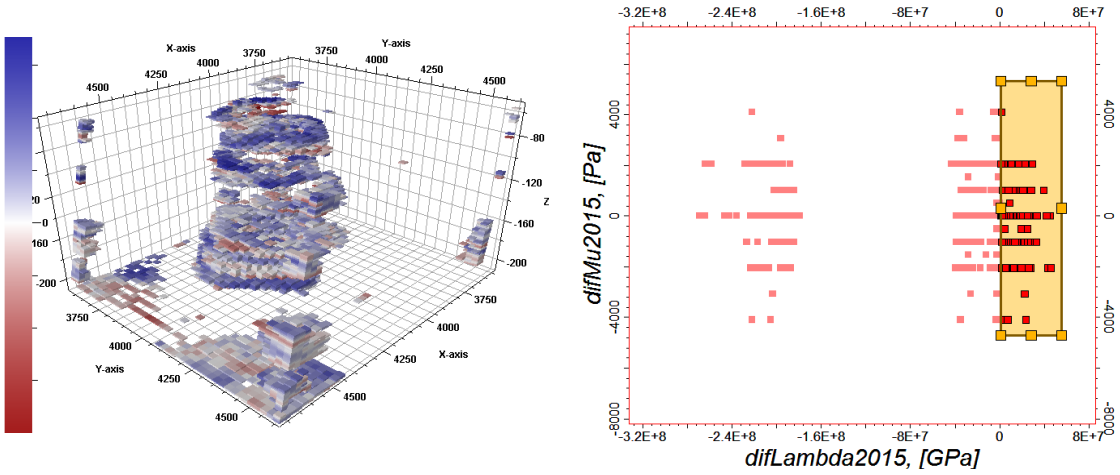

Figure 45: Influence of the gas injection well in the seismic response

The group of cells which present the greatest decrease in **λ** corresponds to the top of the oil leg, where the pressure drop leads to the crossing of the bubble point and the appearance of gas (Figure 46).

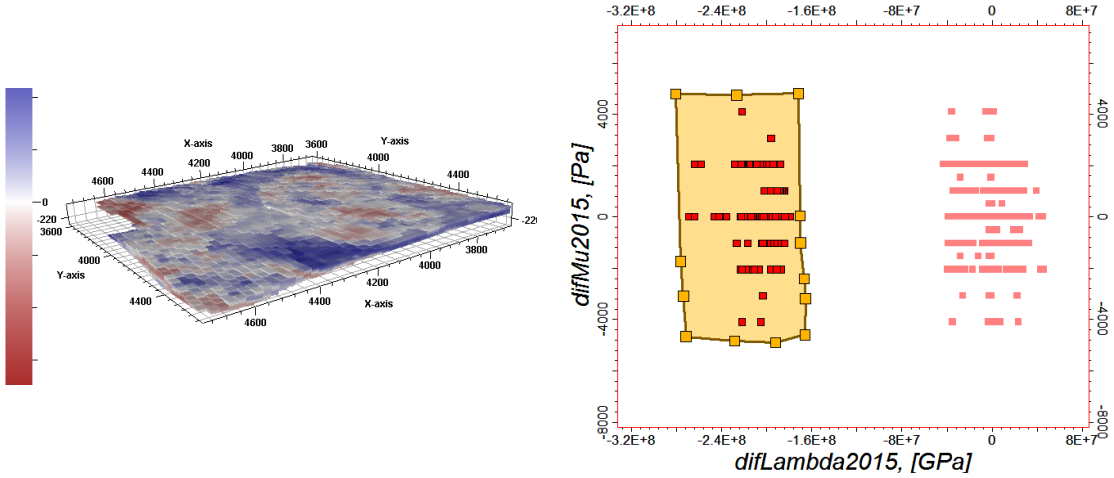

Figure 46: Influence of the gas-oil contact in the seismic response

Figure 47 shows another interesting effect of the production of the reservoir in its seismic trends.

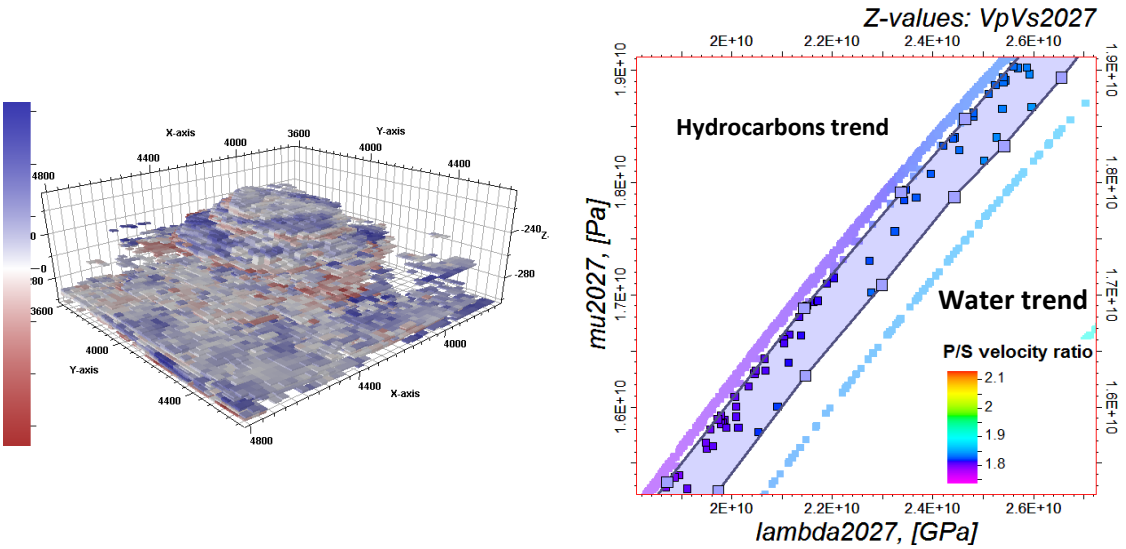

Figure 47: Influence of the water injection in the seismic response

As water is injected into the reservoir and sweeps away the oil, the swept cells start moving towards the water trend. Applying an inclusive filter for these cells to the seismic volume it is possible to identify the swept cells and assess the performance of the water injection.

5. Conclusions

This work has been an attempt to bridge areas often seen as distinct and independent: reservoir modelling, reservoir engineering and geophysics.

The CERENA-I static model was used as a starting point for the construction of a dynamic model to reproduce some specific conditions of a Brazilian Pre-Salt reservoir, and to test reservoir performance and production strategies. Reservoir conditions were borrowed from a real analogue pre-salt field and the equation of state was tuned to match an estimated bubble point and dew point.

The reservoir was produced for thirty two years, from January 2014 to December 2045.The liquid fraction of the gas cap allowed a total production of 2.16×10^5 sm^3 of oil by the end of the first year of production while the oil leg was produced for thirty one years, with a steady production plateau of eighteen years, reaching a total of 6.48×10^6 sm^3 of oil.

The presence of a free gas zone associated with an oil leg indicates that the oil is saturated, or at equilibrium. This implies that any drop in the oil pressure will result in the exsolution of gas. For the oil to flow, a drawdown in the wells is required and in this type of reservoir it is impossible for it to happen without producing very large amounts of gas. The production strategy proved to be able to handle the large quantities of gas produced with little impact in the oil production. This was reached through an efficient gas cycling loop, which was implemented by re-injecting the gas in the centre of the gas cap.

As a final remark on reservoir management, we can see the presence of high amounts of CO_2 in this reservoir as both a problem and an advantage: on the one hand the reservoir will produce large quantities of this gas which will have to be dealt with, increasing surface facilities complexity and production costs; on the other hand the reservoir benefits from a natural enhanced recovery mechanism, as the high content of dissolved CO_2 produces a low viscosity fluid, which greatly facilitates production and increases recovery.

What started as the main objective of this thesis, the construction of a compositional fluid flow dynamic model, gradually became a tool for the construction of a time lapse seismic data set, as the potential of compositional simulation for detailed rock physics modelling was perceived. This rock physics model was then used to compute time-lapse seismic data which was analysed to assess the influence of changes in pore fluids on the seismic response of the model.

The compositional model allowed a detailed tracking of the evolution of pore fluid compressibility and density for each cell. This, together with a rock physics model for the reservoir matrix, was used to compute pre-stack synthetic seismic monitoring data. Unlike unconsolidated sandstone reservoirs, carbonates have high elastic moduli and their overall seismic response tends to be little affected by changes in pore fluid properties. Nevertheless, changes in the seismic response of this reservoir were observed, and directly correlated to the production strategy employed.

As expected, the AVO analysis did not prove to be of relevance in the seismic monitoring campaign as practically no changes occur in the AVO properties throughout the production of this field. On the contrary, the Lamé parameters showed a clear separation of fluid trends and allowed a direct

correlation between the production strategy and the changes in the seismic response of the reservoir, proving in this case to be a good reservoir monitoring tool.

By the end of the first year of production, with the reservoir under natural depletion with gas cycling, the pressure drop led to an increase in gas saturation just under the gas-oil contact, which was manifested in the seismic response as a reduction in the λ parameter. At the same time the re-injected gas created an area around the re-injection well which showed an increase in the λ parameter, caused by the gas acquiring a stiffer behaviour due to compression.

The production of the oil leg also has a visible impact on the seismic response, as the injected water sweeps the oil and induces a stiffer seismic response with swept cells travelling from the oil to the water seismic trend.

As seen in the histograms of differences in seismic amplitudes of the various time steps, most changes in seismic amplitudes occur up to 1%, with few reaching 10% or higher. Whether these changes can be picked up or not in a real seismic campaign will depend greatly on the quality of the whole process, from the acquisition to processing.

Despite the value of time-lapse seismic data shown here, in describing reservoir performance, it is important to stress that this is a noise-free synthetic dataset. In real field data we expect a much weaker seismic response than the one achieved in this case study.

Finally, another interesting fact can also be pointed out from this work, and it relates to the very hot topic in the oil industry that is seismic inversion, in which usually static reservoir properties are inferred from seismic amplitudes. Reservoirs are dynamic systems and, as demonstrated in the previous section, fluid density and saturation can have a direct impact on the seismic response of a reservoir. For this reason, care must be taken when producing inverse models, so as to not interpret seismic amplitudes solely as the influence of static properties when in fact dynamic properties can also play an important role.

6. Future research

George Edward Box once wrote "essentially, all models are wrong, but some are useful". This applies directly to reservoir models as there is always a high degree of uncertainty in producing models of reality based on indirect measurements supported by sparse hard data, and a few educated guesses. This is not so critical in synthetic reservoir models, as there is no specific reality to reproduce, but still efforts should be made to produce ever more realistic models, since they allow the development of new technological tools which can be successfully applied to real case studies.

There are many ways in which this work can be improved and the most obvious one is to start by the static model itself, using better spatial continuity models and joint distributions. The dynamic model can also be improved by using more detailed fluid descriptions, as well as real PVT observations that allow a more sophisticated tuning of the equation of state. The flow simulation could gain more realism with the addition of rock saturation functions from real carbonate reservoirs. The rock physics model could be updated by adding distinct families of pore shapes obtained from models of Micro-Computerized Axial Tomography scanning on real carbonates. The 4D seismic data set could be improved by adding random noise to the amplitudes, to study if the changes during production are significant or fall within the noise variation range.

Despite all the improvements that can be done to this model I believe that, for future work with this data set, it would be much more interesting to try and devise a method of 4D seismic inversion that could tackle both saturation and fluid densities, taking full advantage of the compositional flow simulator.

7. Bibliography

Ahmed, T., & Meehan, D. N. (2012). *Advanced Reservoir Management and Engineering.* Elsevier.

Aki, K., & Richards, P. (1980). *Quantitative Seismology.* Freeman.

Araújo, C. (2013). CO2 injection in Carbonate Reservoirs in Brazil. *Petrobras/CENPES.*

Archilha, N., Missagia, R., Ceia, M., & Neto, I. (2013). Petrophysical, mineralogical and elastic property characterization of Halocene carbonates from Salgada lagoon, Brazil. *SBGf*.

Avseth, P., Mukerji, T., & Mavko, G. (2005). *Quantitative Seismic Interpretation.* Cambridge University Press.

Batzle, M., & Wang, Z. (1992). Seismic properties of pore fluids. *Geophysics*, pp. 1396-1408.

Dake, L. (2001). *The Pratice of Reservoir Engineering (Revised Edition).* Elsevier Science.

Danesh, A. (1998). *PVT and Phase Behaviour of Petroleum Reservoir Fluids.* Elsevier.

Fanchi, J. (2006). *Principles of Applied Reservoir Simulation.* Elsevier.

Jessen, K., Sam-Olibale, L., Kovscek, A., & Orr, F. (s.d.). Increasing CO2 storage in oil recovery. *Department of Petroleum Engineering, Stanford University*.

Lara, A. (2014). Libra PSC, Warming up the engines. *BRATECC Offshore 2014.*

Lohrenz, J., Bray, B., & Clark, C. (1964). Calculating Viscosities of Reservoir Fluids From Their Compositions. *SPE*.

Mavko, G., Mukerji, T., & Dvorkin, J. (2009). *The Rock Physics Handbook.* Cambridge University Press.

McCain, W. D. (1990). *The Properties of Petroleum Reservoir Fluids.* Pennwell Books.

Schlumberger. (2005). *PVTi and ECLIPSE 300 - An Introduction to PVT analysis and compositional simulation.*

Simm, R., & Bacon, M. (2014). *Seismic Amplitude.* Cambridge University Press.

Smith, T., Sondergeld, C., & Rai, C. (2003). Gassmann fluid substitution: A tutorial. *Geophysics*, pp. 430-440.

Kansas Geological Survey (2004). *Sedimentologic and Diagenetic Characteristics of the Arbuckle Group.*

Xu, S., & Payne, M. (2009). Modeling elastic properties in carbonate rocks. *The Leading Edge*, pp. 66-74.

8. Appendices

8.1. Eclipse 300 data file

```
--*******************************************************
RUNSPEC
--project name
TITLE
CERENA 1

COMPS
6 /

REGDIMS
1 1 0 1 0 5 5 /

--grid dimension
DIMENS
45   42   300 /

--Phases
OIL
WATER
GAS

METRIC

WELLDIMS
--  #wells  #connects  #groups  #in_grp  Stages per separator   #Well streams   #Mixtures   #separators   #items in mixture
    6       1*         3       4        5                     1               1           1             1         /                           /

--starting date of the project
START
--  DAY   MONTH  YEAR
    1   JAN  2014 /

--grid definition
GRID

INCLUDE
'actnum.GRDECL' /

INCLUDE
'grid.GRDECL'/

INCLUDE
'poro2.GRDECL' /

INCLUDE
'permx.GRDECL' /

INCLUDE
'permy.GRDECL'/

INCLUDE
'permz.GRDECL' /

GRIDFILE
0 1 /

--*******************************************
INIT

PROPS

INCLUDE
'ZMFVD.PVO' /
```

```
INCLUDE
'CRUDE.PVO' /

INCLUDE
'scal.inc' /

DENSITY
--
-- Fluid Densities at Surface Conditions (Only water density needed, oil and gas densities are calculated)
--
1*  1040.0000    1*/

SOLUTION

--   DATUM          DATUM           OWC       OWC     GOC           GOC
--   DEPTH          PRESS          DEPTH      PCOW   DEPTH          PCOG
EQUIL
--    1            2      3    4      5          6   9  10  11
   209.999815687411    492.9964  300.00  0.00 209.999815687411   0.00  1*   1*    0   3  1/

RPTSOL
FIP=1  PRES  SOIL  SWAT   /

RPTRST

SGAS
SOIL
SWAT
PRES
BO
BOIL
DENG
DENO
PSAT
RS
XMF
YMF
TOTCOMP
/

--*********************************************************************
SUMMARY
--*********************************************************************
FPRP
FOVPR
FOVPT

--Oil
FOPR
FOPT
FOMR
FOMT
FODN

--Gas
FGPR
FGMR
FGMT
FGDN
FGIR
FGIT
FGPT

--Wells
WPI
/
WBHP
/
WWCT
/
```

WOPR
/
WWPR
/
WGPR
/
FGPRB
FGOR
FWIR
FWIT
FWCT
FXMF
1 /
FXMF
2 /
FXMF
3 /
FXMF
4 /
FXMF
5 /
FXMF
6 /
FYMF
1 /
FYMF
2 /
FYMF
3 /
FYMF
4 /
FYMF
5 /
FYMF
6 /
FCMPR
1 /
FCMPR
2 /
FCMPR
3 /
FCMPR
4 /
FCMPR
5 /
FCMPR
6 /
FCMPT
1 /
FCMPT
2 /
FCMPT
3 /
FCMPT
4 /
FCMPT
5 /
FCMPT
6 /
FCMIR
1 /
FCMIR
2 /
FCMIR
3 /
FCMIR
4 /
FCMIR
5 /
FCMIR
6 /

```
FCMIT
1 /
FCMIT
2 /
FCMIT
3 /
FCMIT
4 /
FCMIT
5 /
FCMIT
6 /
FCHMR
1 /
FCHMR
2 /
FCHMR
3 /
FCHMR
4 /
FCHMR
5 /
FCHMR
6 /
FCHMT
1 /
FCHMT
2 /
FCHMT
3 /
FCHMT
4 /
FCHMT
5 /
FCHMT
6 /
FHMPR
FHMPT
FOPRA
FOPRB
FOPTA
FOPTB
FOVPR
FOVPT
FGVPR
FGVPT
FOIP

RUNSUM

EXCEL

--************************************************************
--************************************************************

SCHEDULE

TUNING
/
/
2* 80 /


INCLUDE
'wells2.inc' /

WCONPROD
PROD1  OPEN LRAT 3* 150 1*  350  /
PROD2  OPEN LRAT 3* 150 1*  350  /
PROD3  OPEN LRAT 3* 150 1*  350  /
PROD4  OPEN LRAT 3* 150 1*  350  /
```

```
/
INCLUDE
'injeccao.inc' /

DATES
1 FEB 2014 /
1 MAR 2014 /
1 APR 2014 /
1 MAY 2014 /
1 JUN 2014 /
1 JLY 2014 /
1 AUG 2014 /
1 SEP 2014 /
1 OCT 2014 /
1 NOV 2014 /
1 JAN 2015 /
/
WELSPECS
PROD1   PROD  1   1  200  OIL  1*  STD     /
PROD2   PROD  45  42  200  OIL  1*  STD    /
PROD3   PROD   1  42  200  OIL  1*  STD    /
PROD4   PROD   45  1  200  OIL  1*  STD    /
INJ1    I     20  20  50  GAS  1*  STD   /
INJ2    I     21  21  265  WATER  1*  STD /
/

COMPDAT
--Nome     I    J   Kup   Klow   Open/shut  2*   Well bore     3*     Direcção do poço
PROD1      1    1   1     155    SHUT    2*     0.2         3*         Z /
PROD1      1    1   170   250    OPEN    2*     0.2         3*         Z /
PROD2      45   42  1     155    SHUT    2*     0.2         3*         Z /
PROD2      45   42  170   260    OPEN    2*     0.2         3*         Z /
PROD3       1   42  1     155    SHUT    2*     0.2         3*         Z /
PROD3       1   42  1     250    OPEN    2*     0.2         3*         Z /
PROD4      45   1   1     155    SHUT    2*     0.2         3*         Z /
PROD4      45   1   170   260    OPEN    2*     0.2         3*         Z /
INJ1       20   20  1     150    OPEN    2*     0.2         3*         Z /
INJ2       21   21  170   300    OPEN    2*     0.2         3*         Z /
/

WELOPEN
INJ2  OPEN /
/

CECON
PROD1 4* 0.9 2* CON /
PROD2 4* 0.9 2* CON /
PROD3 4* 0.9 2* CON /
PROD4 4* 0.9 2* CON /
/

DATES
1 FEB 2015 /
1 MAR 2015 /
1 APR 2015 /
1 MAY 2015 /
1 JUN 2015 /
1 JLY 2015 /
1 AUG 2015 /
1 DEC 2015 /
1 FEV 2016 /
1 MAR 2016 /
1 APR 2016 /
1 MAY 2016 /
1 DEC 2016 /
/
DATES
1 MAY 2017 /
1 DEC 2017 /
1 MAY 2018 /
1 DEC 2018 /
```

```
1 MAY 2019 /
1 DEC 2019 /
1 MAY 2020 /
1 DEC 2020 /
1 MAY 2021 /
1 DEC 2021 /
1 MAY 2022 /
1 DEC 2022 /
1 MAY 2023 /
1 DEC 2023 /
1 MAY 2024 /
1 DEC 2024 /
1 MAY 2025 /
1 DEC 2025 /
1 MAY 2026 /
1 DEC 2026 /
1 MAY 2027 /
1 DEC 2027 /
1 MAY 2028 /
1 DEC 2028 /
1 MAY 2029 /
1 DEC 2030 /
1 MAY 2031 /
1 DEC 2031 /
1 MAY 2032 /
1 DEC 2032 /
1 MAY 2033 /
1 DEC 2033 /
1 MAY 2034 /
1 DEC 2034 /
1 MAY 2035 /
1 DEC 2035 /
1 MAY 2036 /
1 DEC 2036 /
1 MAY 2037 /
1 DEC 2037 /
1 MAY 2038 /
1 DEC 2038 /
1 MAY 2039 /
1 DEC 2039 /
1 MAY 2040 /
1 DEC 2040 /
1 MAY 2041 /
1 DEC 2041 /
1 MAY 2042 /
1 DEC 2042 /
1 MAY 2043 /
1 DEC 2043 /
1 MAY 2044 /
1 DEC 2044 /
1 MAY 2045 /
1 DEC 2045 /
/
 END
```

8.2. Include file "crude.PVO"

```
ECHO
-- Units: C
RTEMP
--
-- Constant Reservoir Temperature
--
      100
/

EOS
--
-- Equation of State (Reservoir EoS)
--
  PR3
/

NCOMPS
--
-- Number of Components
--
    6
/
PRCORR
--
-- Modified Peng-Robinson EoS
--
CNAMES
--
-- Component Names
--
  'CO2'
```

```
  'C1'
  'C2'
  'C3'
  'C4-6'
  'C7+'
/
MW
--
-- Molecular Weights (Reservoir EoS)
--
        44.01
       16.043
   30.03651882
       44.097
    70.2371498
          218
/

OMEGAA
--
-- EoS Omega-a Coefficient (Reservoir EoS)
--
  0.457235529
  0.457235529
  0.457235529
  0.457235529
  0.457235529
  0.457235529
/

OMEGAB
--
-- EoS Omega-b Coefficient (Reservoir EoS)
```

```
--
  0.077796074
  0.077796074
  0.077796074
  0.077796074
  0.077796074
  0.077796074
/

-- Units: K
TCRIT
--
-- Critical Temperatures (Reservoir EoS)
--
  250.91111609
  156.9532596
  249.1099632
  304.51896827
  380.6181688
  613.4226548
/

-- Units: bar
PCRIT
--
-- Critical Pressures (Reservoir EoS)
--
  119.1938758
  74.29588135
  78.41736061
  68.83487205
  56.82317979
  27.54568139
```

/

-- Units: m3 /kg-mole

VCRIT

--

-- Critical Volumes (Reservoir EoS)

--

0.09400075621

0.09800017929

0.1470534926

0.1999979608

0.3014148438

0.8499119437

/

ZCRIT

--

-- Critical Z-Factors (Reservoir EoS)

--

0.537080892975933

0.557950389352133

0.55676353303698

0.543743455312942

0.541221410764183

0.459030936952775

/

SSHIFT

--

-- EoS Volume Shift (Reservoir EoS)

--

-0.0453788736841816

-0.182901686008519

-0.126011095016238

-0.105436919693872

0.347695418004011

-0.754778251842114

/

ACF

--

-- Acentric Factors (Reservoir EoS)

--

0.225

0.013

0.09764618515

0.1524

0.224434502

0.70397

/

BIC

--

-- Binary Interaction Coefficients (Reservoir EoS)

--

0.1

0.09817700916 0.003701359105

0.1 0.006214 0.002738293998

0.1 0.01482207968 0.007750716921 0.002218453386

0.1 0.047496 0.03439155849 0.023801 0.0131823004

/

PARACHOR

--

-- Component Parachors

--

```
          78
          77
  106.9094608
       150.3
  225.6184829
   564.40006
/

-- Units: m3 /kg-mole
VCRITVIS
--
-- Critical Volumes for Viscosity Calc (Reservoir EoS)
--
  0.09400075621
  0.09800017929
  0.1470534926
  0.1999979608
  0.3014148438
  0.8499119437
/

ZCRITVIS
--
-- Critical Z-Factors for Viscosity Calculation (Reservoir EoS)
--
  0.537080892975933
  0.557950389352133
  0.55676353303698
  0.543743455312942
  0.541221410764183
  0.459030936952775
/
```

```
LBCCOEF

--

-- Lorentz-Bray-Clark Viscosity Correlation Coefficients

--

   0.1023 0.023364 0.058533 -0.040758 0.0093324

/

ZI

--

-- Overall Composition

--

  0.5497015024

  0.1657320235

  0.04467084702

  0.03158315227

  0.05703144762

  0.1512810272

/
```

8.3. Include file "scal.inc"

```
-- RELATIVE PERMEABILITY AND CAPPILARY PRESSURE CURVES

SWFN


0.2  0.0     0.0

0.3  0.00024  0.0

0.4  0.0039   0.0

0.5  0.02     0.0

0.6  0.062    0.0

0.7  0.152    0.0

0.8  0.316    0.0

0.9  0.585    0.0

1.0  1.0      0.0

/
```

```
SOF3

--So  Kro (oil water regions)  Kro (oil, gas and connate water)

0.1  0.0   0.0

0.2  0.018 0.0

0.3  0.073 0.025

0.4  0.165 0.1

0.5  0.294 0.225

0.6  0.459 0.4

0.7  0.661 0.625

0.8  0.9   0.9

/


SGFN

--Sg Krg Pcog (Gas-Oil Capillary pressure)

0.0  0.0        0.0

0.1  0.0      0.0

0.2  0.018       0.0

0.3  0.073       0.0

0.4  0.165     0.0

0.5  0.294      0.0

0.6  0.459      0.0

0.7  0.661      0.0

0.8  0.9       0.0

/


PVTW

234.46   1.0042   5.43E-05   0.5   1.11E-04   /



-- ROCK COMPRESSIBILITY

--

--    REF. PRES   COMPRESSIBILITY
```

```
ROCK

235         0.00045   /


-- SWITCH OFF OUTPUT OF ALL PROPS DATA


STONE1
```

8.4. Include file "wells2.inc"

```
WELSPECS

PROD1    PROD   1    1  50  OIL    1*   STD     /

PROD2    PROD   45  42  50  OIL    1*   STD     /

PROD3    PROD    1  42  50  OIL    1*   STD     /

PROD4    PROD    45  1  50  OIL    1*   STD     /

INJ1     I      20  20  50   GAS   1*   STD   /

INJ2     I      21  21  265  WATER  1*   STD /

/


COMPORD

-- Nome   Método de ordenação

PROD1   INPUT /

PROD2   INPUT /

PROD3   INPUT /

PROD4   INPUT /

INJ1    INPUT /

INJ2    INPUT /

/


COMPDAT

--Nome     I    J    Kup   Klow   Open/shut  2*   Well bore      3*     Direcção do poço

PROD1      1    1    1     155    OPEN     2*     0.2         3*         Z /

PROD2      45   42   1     155    OPEN     2*     0.2         3*         Z /

PROD3      1    42   1     155    OPEN     2*     0.2         3*         Z /
```

```
PROD4     45   1   1     155    OPEN    2*     0.2        3*         Z /

INJ1      20   20  1     150    OPEN    2*     0.2        3*         Z /

INJ2      21   21  265   300    OPEN    2*     0.2        3*         Z /
```

8.5. Include file "injeccao.inc"

```
WCONINJE

--Nome    Tipo  OPEN/SHUT    Controlo

 INJ1    GAS    OPEN     BHP    2*    530 /

 INJ2    WATER  SHUT     BHP    2*    500 /

/


--WELLSTRE

--Nome da stream    %.1  %2   %3    %4    %5    %6    %7    %8    %9   %10    %11

--  'CO2'           1   0    0     0     0     0    0     0     0    0     0   /

--/


WINJGAS

--Nome  Tipo de fluido injectado    Nome do grupo

INJ1       GV              FIELD   /

/


WAVAILIM
```